Biophysical Journal
Article

Biophysical Society

Role of Phosphorylation in Moesin Interactions with PIP_2-Containing Biomimetic Membranes

Quentin Lubart,[1,2] Helene Vitet,[1,2] Fabien Dalonneau,[1,2] Aline Le Roy,[3] Mathieu Kowalski,[1,2] Morgane Lourdin,[1,2] Christine Ebel,[3] Marianne Weidenhaupt,[1,2] and Catherine Picart[1,2,*]

[1]CNRS UMR 5628 (LMGP), [2]Institut National Polytechnique de Grenoble, and [3]Institut de Biologie Structurale (IBS), University Grenoble Alpes, CEA, CNRS, Grenoble, France

ABSTRACT Moesin, a protein of the ezrin, radixin, and moesin family, which links the plasma membrane to the cytoskeleton, is involved in multiple physiological and pathological processes, including viral budding and infection. Its interaction with the plasma membrane occurs via a key phosphoinositide, the phosphatidyl(4,5)inositol-bisphosphate (PIP_2), and phosphorylation of residue T558, which has been shown to contribute, in cellulo, to a conformationally open protein. We study the impact of a double phosphomimetic mutation of moesin (T235D, T558D), which mimics the phosphorylation state of the protein, on protein/PIP_2/microtubule interactions. Analytical ultracentrifugation in the micromolar range showed moesin in the monomer and dimer forms, with wild-type (WT) moesin containing a slightly larger fraction (~30%) of dimers than DD moesin (10–20%). Only DD moesin was responsive to PIP_2 in its micellar form. Quantitative cosedimentation assays using large unilamellar vesicles and quartz crystal microbalance on supported lipid bilayers containing PIP_2 reveal a specific cooperative interaction for DD moesin with an ability to bind two PIP_2 molecules simultaneously, whereas WT moesin was able to bind only one. In addition, DD moesin could subsequently interact with microtubules, whereas WT moesin was unable to do so. Altogether, our results point to an important role of these two phosphorylation sites in the opening of moesin: since DD moesin is intrinsically in a more open conformation than WT moesin, this intermolecular interaction is reinforced by its binding to PIP_2. We also highlight important differences between moesin and ezrin, which appear to be finely regulated and to exhibit distinct molecular behaviors.

INTRODUCTION

The ezrin/radixin/moesin family of proteins (ERM) is known to play important roles in a large number of fundamental physiological and pathological processes, including cell polarity, division, and metastasis, and formation of protrusions and the immunological synapse (1,2).

Invertebrates mostly express one isoform, whereas the three isoforms are present in vertebrates but with distinct preferential localizations (2). Although their physiological role is somewhat redundant, two ERM proteins can act in concert and complement each other. This is notably the case in the formation of the immunological synapse in leukocytes (3,4), where moesin and ezrin shuttle from the plasma membrane to the cytoplasm, switching between phosphorylation states, during the different steps of the synapse formation process. Both ezrin and moesin are involved in bacterial and viral infections (5–7), phosphorylation of moesin being involved in HIV-1 entry (8–10). Moesin is also involved in the early steps of cancer, such as the formation of invadopodia (11) and tumor cell invasion (12,13), where ezrin and moesin show distinct spatial distributions.

Phosphorylation of ERM proteins by several kinases at different locations on the protein, mostly on threonine, serine, and tyrosine residues (14–16), is an important hallmark of their physiological roles, since it enables them to interact with a large number of cytosolic proteins and with the cytoskeleton (1,17,18). The phosphorylated form is usually considered to be "active" and mainly localized at the plasma membrane, whereas the native "inactive" (unphosphorylated) form is rather localized in the cytosol (19,20).

From a structural point of view, ERM proteins are closely related, with 73% amino acid sequence identity between ezrin and moesin and 76% between ezrin and radixin (2). They contain three important domains: an N-terminal membrane-binding domain (or four-point-one, ezrin, radixin, moesin (FERM) domain), which can bind the plasma membrane via the phosphoinositide phosphatidylinositol(4,5)bisphosphate (PIP_2), a central α-helical linker region, and a C-terminal actin-binding domain (Fig. 1).

Submitted May 1, 2017, and accepted for publication October 17, 2017.

*Correspondence: catherine.picart@grenoble-inp.fr

Editor: Tommy Nylander.

https://doi.org/10.1016/j.bpj.2017.10.041

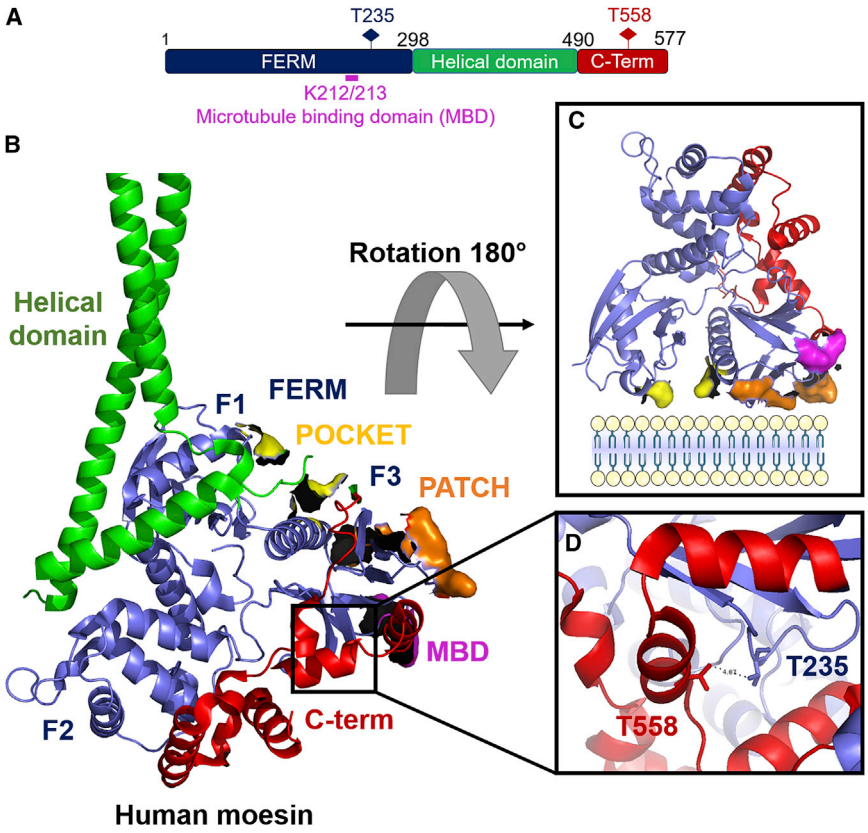

FIGURE 1 Linear and tertiary structure of moesin. All structures were drawn with Pymol software. (*A*) Linear sequence of moesin showing the FERM domain (*blue*), the central helicoidal region (*green*), and the C-terminal domain (*red*). The two mutated phosphorylation sites, T235D and T558D, are shown. The position of the MT binding domain (MBD), K212/213, is also presented. (*B*) 3D structure of moesin from *Spodoptera frugipeda* (PDB: 2I1K) with the positively charged patch (K253/254 and K262/K263) highlighted in orange, the positively charged pocket (K63 and K278) in yellow, and the MBD (K12/213) in purple. (*C*) Zoom on the positively charged patch (K253/254 and K262/K263) highlighted in orange and the positively charged pocket (K63 and K278) in yellow represented close to a lipid bilayer (from PDB: 1EF1). (*D*) The positions of the two mutated T235 and T558 residues, separated by 4.07 Å, are shown (PDB: 1EF1). To see this figure in color, go online.

ERM proteins are characterized by their switch between the closed (also named dormant, autoinhibited, or inactive) conformation, in which FERM and C-terminal domains interact, thus hiding the F-actin-binding region (21), and the open (or active) conformation, in which several interaction sites are unmasked, especially the F-actin binding site at the C-terminus. The interaction with the plasma membrane has been shown to be mediated by binding sites in the FERM domain, which can specifically interact with PIP_2 in the plasma membrane (22,23). Two different binding sites have been identified: a "pocket" containing inositol 1,4,5-trisphosphate in the crystal structure (24) and two pairs of lysine residues (named "patch"), already described as PIP_2-binding sites (Fig. 1) (22,23,25) Recent experimental data highlighted the important role of these two binding sites in the progressive activation of autoinhibited moesin at the membrane (26).

Phosphorylation of ERM proteins is also thought to be involved in a second conformational change (23) by increasing the repulsive interactions between the FERM domain and the C-terminal domain due to the negative charge of the additional phosphate group. Indeed, the two major phosphorylation sites being T558 in the C-terminal domain and T235 on the F3 lobe of the FERM domain, their phosphorylation may contribute to an important functional conformational change of the protein.

To study ERM/plasma membrane interactions in well-defined and simplified conditions, different types of biomimetic lipid membranes containing PIP_2 have been developed and studied with recombinant ERM proteins (27). Large unilamellar vesicles (LUVs) are probably the most popular, since they enable us to quantify the binding affinity of ERM to the PIP_2-containing membranes (26,28,29). Giant unilamellar vesicles (GUVs) are of cell size (30,31) but more difficult to control, whereas supported lipid bilayers (SLBs) can be used for real-time and kinetic studies (32–34). To date, the role of phosphorylation in ERM/PIP_2-containing membrane interactions has barely been explored in vitro, and for ezrin only a phosphomimetic mutant, T567D, has been characterized (34,35). To our knowledge, the role of a double phosphomimetic mutation, T235D/T558D, in moesin has never been studied.

In this work, our aim was to understand the precise role of phosphorylation in the molecular interactions between moesin and PIP_2-containing membranes, especially LUVs and SLBs. To this end, we produced a double phosphomimetic mutant, T235D/T567D (hereafter called DD moesin), that mimicks the fully phosphorylated form of the protein (16,21) and employed complementary biophysical techniques to identify the mechanisms of these interactions. Analytical ultracentrifugation provided insight into the conformational state of the wild-type (WT) and DD moesin

in solution, whereas quantitative cosedimentation assays, intrinsic fluorescence of tryptophan, and quartz-crystal microbalance with dissipation monitoring enabled us to quantify the molecular interactions. We found that the double phosphomimetic mutant exhibited a specific and cooperative interaction with PIP_2-containing membranes that is sensitive to the sequence of adsorption events and leads to the formation of surface-bound DD moesin oligomers. Furthermore, only DD moesin was able to interact with microtubules (MTs), confirming its open conformation once adsorbed.

MATERIALS AND METHODS

Reagents

PIP_2 (purified from porcine brain with a fatty acid composition primarily composed of 18:0, 18:1, and 20:4 acyl chains), 1-oleoyl-2-(6-(4-(dipyrrometheneboron difluoride)butanoyl)amino)hexanoyl-*sn*-glycero-3-phosphoinositol-4,5-bisphosphate (ammonium salt) (TopFluor PI(4,5)P_2), 1-palmitoyl-2-oleoyl-*sn*-glycero-3-phospho-L-serine (POPS), and 1-palmitoyl-2-oleoyl-*sn*-glycero-3-phosphocholine (POPC) were obtained from Avanti Polar Lipids (Alabaster, AL). All compounds for buffer preparations were purchased from Sigma-Aldrich (St. Louis, MO).

Protein expression and purification

For the double mutation, two threonine residues were replaced by two aspartic acid residues (T235D and T558D), and the resulting protein is hereafter called DD moesin. Site-specific mutations were made using the QuickChange II XL site-directed mutagenesis kit (Agilent Technologies, Santa Clara, CA). The constructs were verified by sequencing. WT and mutant (DD) moesin were produced and purified from *Escherichia coli* as previously described (29). Briefly, a GST-tagged recombinant moesin gene was cloned into the pGEX2-T vector and transformed into Rosetta 2 (*E. coli*) bacteria. Bacteria were routinely grown in Luria Bertani medium supplemented with 500 mM NaCl, 100 μg/mL ampicillin, and 34 μg/mL chloramphenicol. Protein expression was induced with IPTG (0.5 mM) at an $OD_{600\ nm}$ of 0.6, and bacteria were harvested by centrifugation after overnight incubation and lysed by ultrasound in phosphate-buffered saline (pH 7.4), 10 mM EDTA, and 0.5 mM dithiothreitol (DTT) buffer. After removal of the bacterial debris, the bacterial lysate was incubated with 5 mL glutathione sepharose beads (GE Healthcare, Little Chalfont, United Kingdom) for 2 h at 4°C. The beads were washed to eliminate non-bound proteins. Moesin was removed from the beads by cleaving the GST moiety with thrombin (2 U/μL) (T7009; Sigma-Aldrich) in Tris buffer (20 mM Tris-HCl (pH 7.4), 100 mM NaCl, and 0.5 mM DTT) for 2 h at 4°C. The protein was then dialyzed against a Mes buffer (20 mM NaCl and 25 mM 2-(N-morpholino)ethanesulfonic acid (MES)) at pH 6.2. The yield of protein was 4–5 mg per liter of bacterial culture. WT and DD moesin were stable at 4°C for ~3 weeks. For the experiments, the buffer was brought to pH 7.4 with a Tris buffer (30 mM Tris at pH 8) containing 0.5 mM EGTA, and the protein was finally placed in a MES-Tris buffer at pH 7.4.

Tubulin purification and labeling, and MT preparation

Tubulin was purified and labeled as previously described (36). MTs were polymerized by mixing tubulin (80%) and ATTO-565-labeled tubulin (20%) in the presence of 1 mM GTP in a Pipes buffer (80 mM Pipes (pH 6.8), 1 mM EGTA, and 1 mM $MgCl_2$) with 1 mM DTT at 37°C for 1 h. Afterward, MTs were incubated with 10 μM of Taxol to stabilize them and prevent their depolymerization (37).

Analytical ultracentrifugation

Experiments were performed using a Beckman XL-I analytical ultracentrifuge (AUC) with an AN-50 TI rotor (Beckman Instruments, Brea, CA), at 20°C and 42,000 Rpm, using 400 μL samples loaded into two-channel 1.2 cm path-length centerpieces with sapphire windows (Nanolytics, Potsdam, Germany). The absorbance at 280 nm was monitored every 11 or 15 min with a 30 μm radial step size. The samples were prepared in MES-Tris buffer. The experiments were done with WT or DD moesin alone at 2 or 8 μM, or at 8 μM in the presence of 100 μM of PIP_2, which is micellar at this concentration (38). The partial specific volumes (v) of WT and DD moesin were estimated from their amino acid compositions to be 0.732 and 0.736 cm^3/g, respectively, and their molecular masses (MM) were estimated to be 67,800 and 135,600 Da for the monomer and dimer of the two constructs, using *the* SEDFIT software (available free at https://sedfitsedphat.nibib.nih.gov). Solvent viscosity, $\eta = 1.035$ mPa.s, and density, $\rho = 1.005$ g/cm^3, were estimated using the SEDNTERP software (available free at http://sednterp.unh.edu/). These values were used to correct the sedimentation coefficient values, s, as s_{20w} values. Each set of sedimentation velocity profiles was globally analyzed, considering typically 30 experimental profiles acquired over 6.5 h, using the size distribution, $c(s)$, and non-interacting species analysis methods (39) embedded in the SEDFIT software. The $c(s)$ analysis was performed with a 0.68 confidence level for the regularization. We considered 200 particles with different sedimentation coefficients, s, and fitted a common frictional ratio, f/f_{min} (a mean operational value that is not further considered). The s values of the peaks of the $c(s)$ distribution were used to determine the weight percent (wt %) of the different species and, considering the protein as a monomer or a dimer for determination of MM, to calculate the frictional ratio $f/f_{min} = R_H/R_{min}$, where R_H is the hydrodynamic radius and R_{min} the radius of the anhydrous volume, using the Svedberg equation:

$$s = \frac{MM(1-\rho\bar{v})}{N_A 6\pi\eta R_H}. \quad (1)$$

The non-interacting species analysis allowed us to fit the s and MM values of the moesin main species.

Preparation of LUVs and small unilamellar vesicles

LUVs made of POPC, POPC/PIP_2 95/5 (w/w), and POPC/PS 80/20 (w/w) were prepared by drying the appropriate lipid mixture in a Speedvac rotary evaporator (Eppendorf, Hamburg, Germany) and hydrating the lipids with the appropriate buffer for 1.5 h at 37°C. Lipid emulsions were then submitted to extrusion through a stack of two polycarbonate filters (100 nm pore diameter, 21 passages) using a mini-extruder (Avanti Polar Lipids). Small unilamellar vesicles (SUVs) were prepared by an additional extrusion step (21 passages) through a stack of two polycarbonate filters of 50 nm pore diameter. LUVs and SUVs were stored at 10 and 1 mg/mL total lipid concentration, respectively, for no more than 2 days at 4°C. Tris buffer (10 mM Tris (pH 7.4), 100 mM NaCl, and 0.5 mM EGTA) and citrate buffer (10 mM citrate (pH 4.6), 100 mM NaCl, and 0.5 mM EGTA) were used for experiments in physiological and acidic pH, respectively.

Dynamic light scattering and ξ-potential measurements

The homogeneity in size and charge of the vesicles was checked by dynamic light scattering (DLS) and ξ-potential measurements, respectively,

using a Zeta Sizer NanoZS (Malvern Instruments, Worcestershire, United Kingdom). The electrophoretic mobility of LUVs was measured at lipid concentrations of 0.1 mg/mL in a Hepes-NaCl buffer (20 mM Hepes (pH 7.4), 50 mM KCl, and 0.5 mM EDTA) and the ξ-potential at SUV concentrations of 1 mg/mL in a 10-times-diluted Hepes-KCl buffer. This potential which is the electrostatic potential at the shear plane, was calculated using the Helmholtz-Smoluchowski equation (Eq. 2) (40):

$$\xi = \frac{u\eta}{\varepsilon_0 \varepsilon_R}, \tag{2}$$

where ξ is the ξ-potential of a vesicle (in mV); u is the velocity of the vesicle in a unit electric field; η is the viscosity of the aqueous solution; ε_R is the dielectric constant of the aqueous solution; and ε_0 is the permittivity of free space. The ξ-potential is proportional to the surface charge density (40).

Cosedimentation assays

The affinity constant of moesin for LUVs was determined by cosedimentation assays with sucrose-loaded LUVs, as previously described for ezrin (28). Sucrose-loaded LUVs were prepared in a Hepes-sucrose buffer (25 mM Hepes (pH 7.4), 200 mM sucrose, and 1 mM EDTA) and the cosedimentation assays were performed in Hepes-KCl buffer (25 mM Hepes (pH 7.4), 100 mM KCl, and 1 mM EDTA) by varying the total concentration of lipid while keeping constant the percentage of PIP_2 in the LUVs. For these experiments, the moesin concentration was kept constant at 0.4 μM. After incubation for 15 min at room temperature, the 100 μL samples were centrifuged at 16,000 $\times$ g for 1.5 h at 4°C. The top 80 μL of each sample was removed, supplemented with 10 μL 0.2% Triton, and considered as the supernatant. 10 μL of 0.2% Triton and 60 μL of Hepes-KCl buffer were used to resuspend the remaining 20 μL of pellet (P). SN and P were analyzed on a 10% sodium dodecyl sulfate polyacarylamide gel (SDS-PAGE) stained with Coomassie blue. Quantification was achieved using Image J 1.36b (National Institutes of Health, Bethesda, MD) (the mean density of each band was background corrected and checked to make sure it was in the linear range of the scanner). Since 20 μL of the supernatant was counted as pellet and since the supernatant and pellet resuspension volume were identical, the true pellet intensity was calculated using the formula $I_{Pellet} = I_{measured} - 0.25 \times I_{SN}$, where I_{Pellet} and I_{SN} are the intensity values of the pellet and supernatant, respectively. The corresponding percentage of protein bound was calculated as $I_{Pellet} \times 100/(I_{Pellet} + I_{SN})$. The experimental data were fitted using the equation

$$\frac{[M]_B}{[M]_B} = \frac{K \times [PIP_2]^n_{[ACC]}}{1 + K \times [PIP_2]^n_{[ACC]}}, \tag{3}$$

where $[M]_B$ and $[M]_T$ are the bound and total Moesin, respectively, and $[PIP_2]_{ACC}$ is the accessible PIP_2 concentration. It is assumed here, in a first approximation, that all PIP_2 on the outer leaflet of the membrane is accessible. n is the Hill coefficient ($n = 1$ when there is no cooperativity and $n > 1$ in the presence of positive cooperative interactions). The association constant, K, deduced from Eq. 3 is the reciprocal of the apparent dissociation constant, which is often called the affinity constant, K_d.

Spectroscopic measurement of intrinsic fluorescence of tryptophan

Tryptophan fluorescence emission spectra of WT moesin and DD moesin at 0.4 μM were recorded in the absence of PIP_2-LUVs or after addition of increasing amounts of PIP_2-LUVs (corresponding to 1, 1.7, 2.3, and 2.9 mg/mL, respectively, of total lipids) using a TECAN infinite 1000 fluorescence spectrometer (TECAN, Männedorf, Switzerland). For intrinsic fluorescence, a Hellma 96 quartz 96-well plate was used and the excitation and emission wavelengths were set to 280 $\pm$ 5 and 333 $\pm$ 5 nm, respectively). The measurements were made after 45 min of incubation in the dark, each spectrum being the average of at least nine independent measurements. The percentage of quenching was calculated by the equation

$$\%\ \text{of quenching} = [(\text{Fluo}_{\text{moesin}} - \text{Fluo}_{\text{moesin+LUVs}}) \times /\text{Fluo}_{\text{moesin}}] \times 100, \tag{4}$$

where Fluo is the fluorescence intensity (in arbitrary units).

Quartz-crystal microbalance with dissipation monitoring experiments

Quartz-crystal microbalance with dissipation (QCM-D) sensors coated with a silica coating (50 nm SiO_2; QSX303, Biolin Scientific, Västra Frölunda, Sweden) were cleaned. First, they were rinsed for 30 min in 2% (w/v) SDS, then with ultrapure water, before being dried under a nitrogen stream. Finally, they were exposed for 10 min to an ultraviolet/ozone treatment (Jelight Company, Irvine, CA). The preactivated sensors were added in the QCM chambers and rinsed with ultrapure water followed by citrate buffer for 20 min. Then SUVs at 0.1 mg/mL were incubated at 21°C, to enable spreading of the lipids on the underlying substrate. After bilayer preparation, the citrate buffer at pH 4.6 was exchanged for a Tris buffer at pH 7.4.

QCM-D experiments were done at 21°C on an E4 apparatus (QCM-D Q-Sense, Biolin Scientific). The flow chambers were connected to a peristaltic pump (Ismatec IPC, Glattbrugg, Switzerland). Frequency and dissipation shifts of the third, fifth, and seventh overtone of the sensor's resonance frequency (5 MHz) were recorded.

After stabilization of the baseline, the neutralized protein in MES-Tris buffer was injected at different concentrations. We performed two different sets of experiments. In the first type, a total protein volume of 200 μL was microinjected at a 200 μL/min flow for 55 s. After reaching a plateau value, the adsorbed protein layer was rinsed. In the second type of experiment, the protein was injected at a continuous flow rate of 10 μL/min until a plateau value was reached. For MT experiments, the moesin proteins were injected at 16.7 μM for WT and 26.8 μM for DD in two successive injections before being rinsed. Then, MTs were injected under a constant flow rate of 10 μL/min in the chamber in MES-Tris buffer supplemented with 10 μM Taxol.

Total internal reflection fluorescence experiments

For total internal reflection fluorescence (TIRF) experiments, clean glass coverslips were used (thickness 0.13 mm; Marienfeld, Lauda-Königshofen, Germany). Cleaning was achieved in a way similar to that for the QCM sensor, except for the last step, where ultraviolet/ozone was replaced by a 20-min activation with 14 M NaOH. Finally, the coverslips were rinsed with ultrapure water and dried under an argon stream. A silicone insulator (P24742, Molecular Probes, Eugene, OR) was then glued to prepare several individual microwells. Then, 2 μL of SUVs at 1 mg/mL in citrate buffer were adsorbed for 1 h. They were finally thoroughly rinsed with citrate and Tris-buffer.

The proteins in the MES-Tris buffer at pH 7.4 were injected at 7.4 μM for WT and 17.8 μM for DD in three separate injections by removing and adding 10 μL volumes with a period of 30 min between each injection. After the last injection of proteins, the proteins were left to adsorb for 1 h on the SLB. Then, they were rinsed three times with MES-Tris buffer containing 10 μM Taxol and left to adsorb for 30 min before the injection of MTs (single injection at 25 μM). After 1 h of adsorption, they were rinsed with MES-Tris buffer.

Data representation

For the formation of SLBs, the data are presented as box plots (first quartile, median, and third quartile, the limits being 10 and 90% and the extreme values 5 and 95%, respectively). Experiments were performed at least four times, with at least two samples per condition in each experiment.

RESULTS

Structure of WT and DD moesin and interaction sites with PIP_2

From a structural point of view, moesin contains three important domains: an N-terminal membrane-binding domain (FERM domain), which can bind the plasma membrane via phosphatidylinositol (4,5)-bisphosphate (PIP_2), an α-helical linker region, and a C-terminal actin-binding domain (Fig. 1, *A* and *B*). Membrane binding to PIP_2 (41) is recognized as a key step in ERM activation (22,23,25) and in ERM localization at the plasma membrane (3,42). However, the precise molecular mechanisms of this activation and the exact role of phosphorylation in this process are not completely understood. Phosphorylation is also thought to be involved in a second important step (23,26). In moesin, the major phosphorylation sites involved in the conformational change are T235 and T558 (Fig. 1, *A* and *D*). These residues were mutated into aspartic acid (T235D, T558D) to mimic in vitro the phosphorylation (phosphomimetic mutant, DD moesin). The quality control after production and purification of DD moesin was done by mass spectrometry (Figs. S1 and S2).

Oligomerization state of WT and DD moesin in solution studied by AUC

We first studied the sedimentation velocity of WT and DD moesin by AUC (Fig. 2), which provides information on the presence of monomers, dimers, and multimers in solution (43,44). The proteins were either alone in solution at 2 or 8 μM or in the presence of micellar PIP_2. Representative experimental curves for the sedimentation coefficient are given for WT and DD moesin, revealing the presence of two major characteristic peaks, s_1 at ~3.8 S (s_{20w} ~4 S) and s_2 at ~5.4 S (s_{20w} ~5.7 S) (Fig. 2, *A* and *A'*). We attributed these two peaks to the monomer (f/f_{min} = 1.45) and dimer (f/f_{min} = 1.6), which was confirmed by the noninteracting species analysis, providing an MM of 69 ± 2 and 143 ± 20 kDa, respectively (45). f/f_{min} is representative of the shape of the protein, with a value of 1.25 being typical for a globular compact protein, whereas $f/f_{min} > 2$ indicates a fiber or a noncompact structure. Our results suggest that the dimeric form of moesin is slightly more elongated than the monomeric form.

About two-thirds (65–68%) of WT moesin in solution was monomeric, whereas one-third (29–31%) formed dimers, with negligible (<4%) amounts of larger multimers

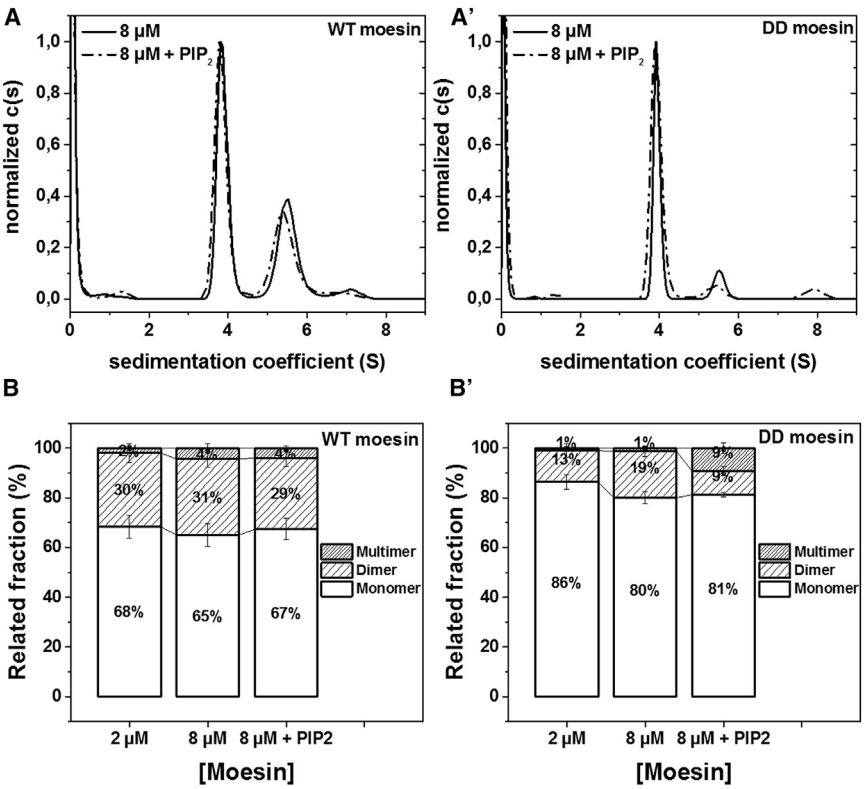

FIGURE 2 AUC of WT and DD moesin in solution in the absence and presence of PIP_2. (*A* and *A'*) Representative *c*(*s*) distributions obtained for WT (*A*) and DD moesin (*A'*) showing the presence of two characteristic peaks, s_1 ~3.8 S and s_2 ~5.4 S. These were attributed to the monomeric and dimeric forms of moesin, respectively. (*B* and *B'*) Relative fractions, expressed in percentages, of monomers, dimers, and larger species for WT moesin (*B*) (error bars represent SD for $n = 4$ independent experiments) and DD moesin (*B'*) ($n = 3$ independent experiments) at increasing concentrations and in the presence of PIP_2 added at 100 μM.

(Fig. 2 *B*). The concentration of protein (investigated at 2 and 8 μM) did not change this distribution. Furthermore, PIP_2 did not affect WT moesin oligomerization. In contrast, for DD moesin, the percentage of monomers was higher (86%) at low protein concentration (2 μM) and decreased slightly to 80% when the DD concentration increased to 8 μM, the fraction of dimers following the reverse trend, with insignificant amounts of larger multimers (1%). In the presence of 100 μM PIP_2, at 8 μM DD, the fraction of monomers remained stable and the fraction of species larger than dimers, presumably bound to PIP_2 micelles, notably increased from 1 to 9% at the expense of dimers (Fig. 2 *B'*).

Altogether, these results show that WT moesin has a significantly higher fraction of dimers than the phosphomimetic mutant. Besides, WT moesin is rather insensitive to PIP_2 in solution, whereas DD moesin can interact with micellar PIP_2.

To compare the affinities between the proteins and PIP_2, we used co-sedimentation assays (28) and measured the dissociation constant (K_d) between the protein and PIP_2-LUVs. We recently determined this K_d value for ezrin (28) and for WT moesin (29). To this end, increasing concentrations of sucrose-loaded PIP_2-LUVs were incubated in a buffer containing WT moesin at a fixed concentration (0.4 μM). Centrifugation allows separation of the LUV-bound moesin in the pellet from the soluble protein in the supernatant. Typical images of SDS-PAGE gels representing the pellets and the supernatants are shown in Fig. 3, *A* and *B*, for increasing lipid concentrations interacting with WT and DD moesin, respectively. In Fig. 3, *A*' and *B'*, the percentage of moesin bound is represented as a function of the accessible acidic lipid concentration. We found that the percentage of bound moesin increased with increasing amounts of PIP_2-LUVs. The fit of the experimental data using a 1:1 interaction model gives a $K_d = (7.8 \pm 0.9)$ μM for WT moesin, close to the previously published value, $K_d = (5.6 \pm 0.7)$ μM (29), and similar to the one determined for other ERM proteins (ezrin $K_d = 5.9 \pm 0.7$ μM (28)). In contrast, DD moesin interacted cooperatively with PIP_2-LUVs, since a 1:1 interaction model did not adequately fit the data, whereas a cooperative interaction did (Fig. 3 *C*, Hill coefficient of 2.4). The specificity of WT and DD moesin interactions with PIP_2 was assessed by studying their interaction with LUVs composed of POPC and POPC/POPS (80/20), another negatively charged lipid constituting the inner leaflet of the plasma membrane (46). The lipid composition percentages were chosen, since a composition of POPC/POPS of 80:20 mol % is a commonly used simple model of the inner lipid leaflet of a plasma membrane (47). In addition, it has previously been reported that PIP_2 has a net charge of -3 due to the phosphate groups (each phosphate group bearing more than one negative charge) and that POPS has a net charge of -1 (the COO- group bearing one negative charge) (48). The surface area of the respective headgroups are also different, the surface area of the PIP_2 headgroup being 1.1 nm^2 (49), whereas that of POPS is 0.62 nm^2 (50).

Both WT and DD moesin lack affinity for pure POPC LUVs (Fig. 3, *A–C*, *solid* and *open circles*, respectively) and exhibited a very low affinity, of electrostatic origin, for POPS-LUVs (*solid* and *open squares*, respectively) at 54.4 $\pm$ 5.8 and 44.7 $\pm$ 5.2 μM, respectively.

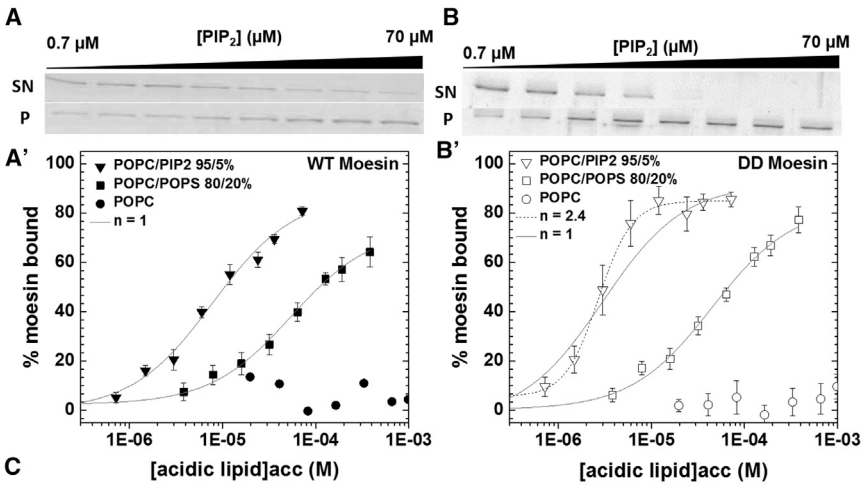

C

Membrane	WT Moesin (µM)	DD Moesin (µM)
POPC/POPS	54.3 ± 5.8	44.7 ± 5.2
POPC/PIP_2	7.8 ± 0,9	2.7 ± 0.1 (n=2.4)

FIGURE 3 Quantitative cosedimentation assays of WT and DD moesin binding to PIP_2 and POPS-LUVs. SDS-PAGE analysis of pellet (P) and supernatant (SN) of WT moesin (*A*) and DD moesin (*B*) at 0.4 μM after interaction with increasing amounts of PIP_2-LUVs (95/5 POPC/PIP_2). (*A'*) Percentage of WT moesin bound to LUVs as a function of the concentration of acidic lipids PC/PIP_2, 95/5 (*solid inverted triangles*), where the *X* axis is the accessible concentration in PIP_2 (respectively POPS), $[PIP_2]_{acc}$, calculated assuming that the PIP_2 molecules are equally distributed in the two membrane leaflets and that only the molecules in the outer leaflet are accessible to the proteins; PC/POPS, 80/20 (*solid squares*), where the *X* axis is the accessible concentration in PS, $[PS]_{acc}$; and PC (*solid circles*), where the *X* axis is the accessible lipid concentration. The curves are the least-squares fits of the data, which yield the value of the affinity constant, K_d (points are represented as the mean $\pm$ SD of at least three independent experiments). Similar data are given for DD moesin (*B'*) with open symbols. (*C*) K_d values obtained for WT and DD moesin interactions with POPS and PIP_2-LUVs. n represents the Hill coefficient. To see this figure in color, go online.

It should be noted that we also measured the intrinsic fluorescence of tryptophan residues in WT and DD moesin by absorbance spectroscopy (Fig. S3) to further evaluate the effect of PIP_2-LUV binding. First, we did not detect any shift in the position of the maximum emission wavelength. We found that the quenching of intrinsic fluorescence in WT moesin or DD moesin was systematically and significantly higher after addition of PIP_2-LUVs than after addition of POPC-LUVs. However, quenching was globally similar for both proteins, but with a slightly stronger increase with PIP_2-LUVs for DD moesin compared to WT moesin. Thus, our measurements indicate a specific effect of membrane binding on the environment of intrinsic protein fluorophores and a slightly higher sensitivity for DD moesin in comparison to WT moesin.

Characterization of PIP_2-SUVs and formation of PIP_2-SLBs

After having confirmed the specific interaction of WT and DD moesin with PIP_2-LUVs, we further studied the interaction of moesin and its phosphomimetic mutant with SLBs by QCM, a technique allowing real-time investigation of molecular interactions (51,52). Formation of SLBs can be achieved by fusion of SUVs on the surface, a process that needs to be optimized depending on the vesicle lipid composition, since negatively charged lipids are known to be less prone to rupture on a negatively charged silica surface (53–55). Indeed, QCM-D experiments related to SLBs are usually performed on a preactivated silica crystal. Calcium ions are usually added to help vesicle rupture and formation of SLBs. However, since Ca^{2+} ions have a particularly high affinity for PIP_2 (56,57) and can destabilize PIP_2-membranes (30), one of the requirements for our experiments was to avoid Ca^{2+} ions in the buffer. Unfortunately, the high negative charge of PIP_2 provided by its two phosphate groups is already known to impede the formation of planar membranes such as GUVs and SLBs (55). Recent experiments have shown that decreasing the pH of the buffer used for vesicle rupture from 7.4 to an acidic pH facilitates the formation of SLBs (33,58).

The first step was thus to assess the effective formation of PIP_2-SLBs. The PIP_2-SUVs were extruded from PIP_2-LUVs after passage through 50-nm-diameter porous membranes. Their ζ-potential was measured at pH 4.6 and 7.4 with different concentrations of PIP_2, and the size of the SUVs was measured by DLS (Fig. 4). As expected, the ζ-potential of the PIP_2-SUVs decreased when the percentage of PIP_2 in the SUV increased (Fig. 4 *A*). The ζ-potential also increased when the PIP_2-SUVs were formed in the acid buffer at pH 4.6, its value increasing from -39 ± 10 to -17 ± 2 mV for 4% PIP_2-SUVs when the pH decreased from 7.4 to 4.6, respectively. Importantly, the mean size of the SUVs remained in the range 73–80 nm and was not affected by the pH change nor by the percentage of PIP_2 in the membrane (Fig. 4 *B*).

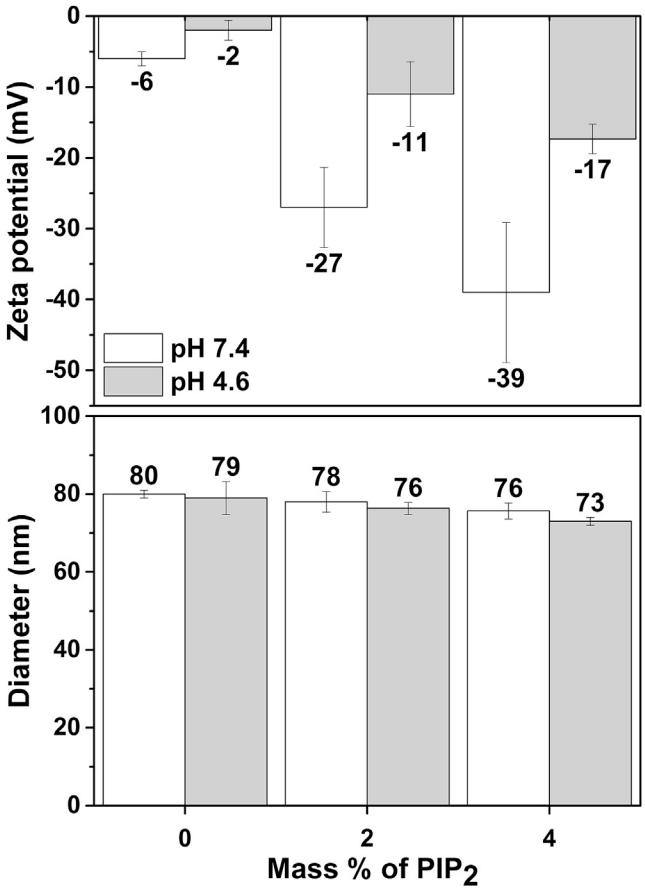

FIGURE 4 ζ-potential measurements and diameter of PIP_2-SUVs. The ζ-potential (in mV) was measured on PIP_2-SUVs at two pH values (4.6 and 7.4; *gray* and *white bars*, respectively) for increasing concentrations of PIP_2 in the lipid membrane (0, 2, and 4%). The diameter of the PIP_2-SUV (in nm) is given for the same experimental conditions (values represent the mean ± SD of $n = 3$ independent experiments)

The formation of the PIP_2-SLBs was next followed by QCM-D (Fig. 5). The frequency shift (Fig. 5 *A*) and dissipation shift (Fig. 5 *A'*) during SLB formation, corresponding to the rupture of SUVs, have been well documented for DOPC/DOPS membranes (52) but have barely been studied in detail for more complex, negatively charged lipids such as phosphoinositides, especially PIP_2 (55). In Fig. 5, the peak in frequency shift reached during the formation of SLBs is followed by a plateau at a characteristic level. The values of the peak in frequency shift, the plateau, and the corresponding dissipations are plotted for SLBs of different composition in Fig. 5, *B* and *B'*, for PIP_2-SLBs at 4% and pure POPC membranes, respectively. Fig. 5, *C* and *C'*, show the values measured during the formation of PIP_2-SLBs at increasing percentages of PIP_2 compared to membranes containing 20% (in mass) POPS.

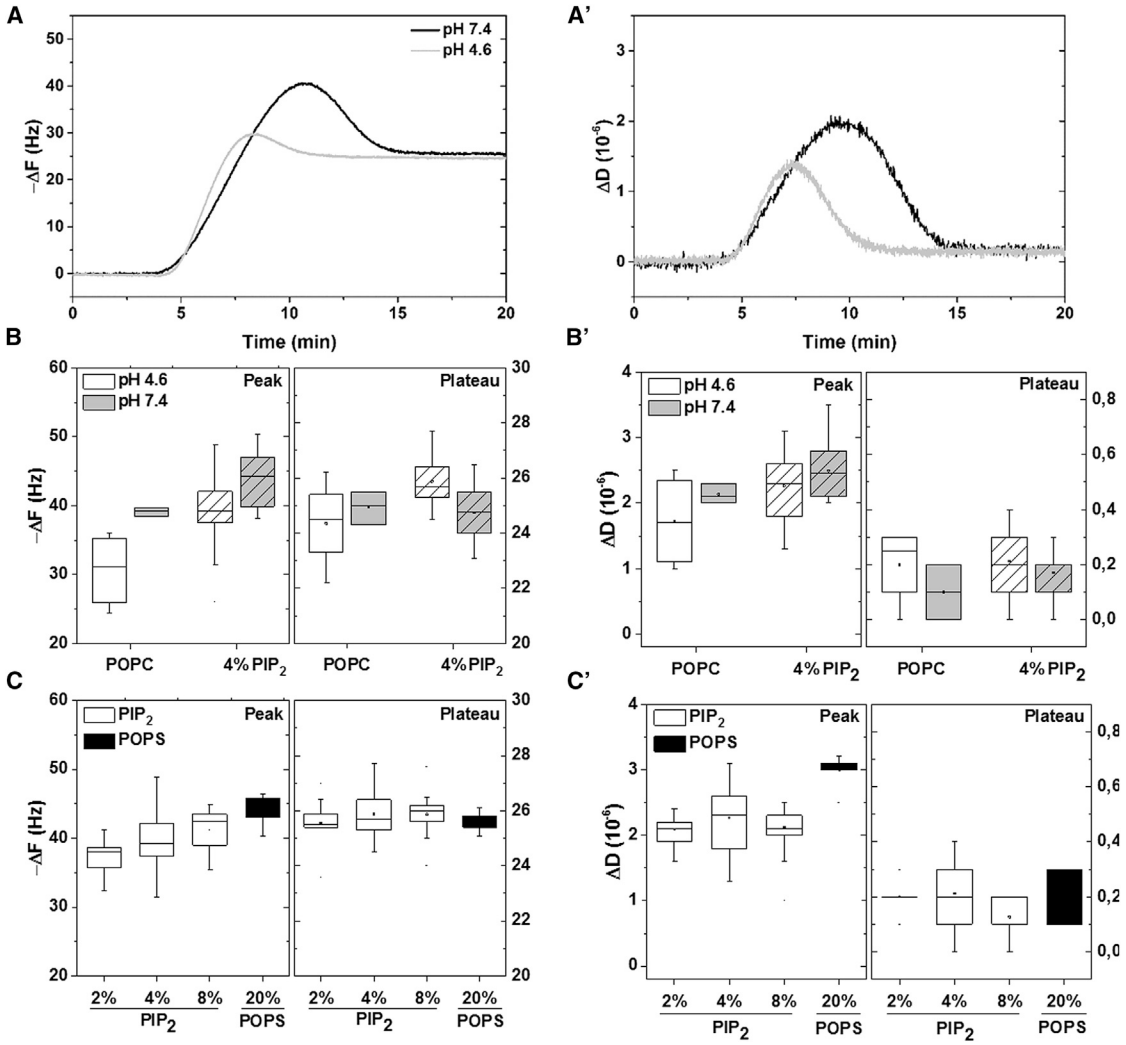

FIGURE 5 Formation of PIP_2-SLBs and POPS-SLBs followed by QCM-D monitoring as a function of pH and acidic lipid composition. (*A* and *A'*) Representative experimental curves during in situ formation of a 4% PIP_2-SLB showing the time evolution of the frequency (*A*) and dissipation (*A'*) at pH 7.4 and 4.6. (*B*) Peak and plateau in ΔF obtained for pure POPC-SLBs and 4% PIP_2-SLBs at pH 4.6 (*gray bars*) and 7.4 (*white bars*). (*B'*) Corresponding dissipation shifts at the peak and plateau values. (*C*) Peak and plateau values in ΔF obtained for pure PIP_2-SLBs at increasing concentrations of PIP_2 from 2 to 8% and for POPS at 20%. (*C'*) corresponding dissipation shifts at the peak and plateau values. For (*B*), (*B'*), (*C*), and (*C'*), data are represented as box plots (representing $n = 3$–40 independent experiments, depending on the conditions).

As anticipated, we can see that the peak values for POPC, both in frequency shift and dissipation, are lower than those of 4% PIP_2-membranes and also lower when the pH is decreased to 4.6 instead of 7.4 (Fig. 5, *B* and *B'*). Once the SLB is formed, however, these values are very close to one another, proving that the SLBs have formed effectively in all these experimental conditions (59). The diffusion of PIP_2 in the membrane is not affected by the pH (4.6 or 7.4), as documented by fluorescence recovery after photobleaching experiments in acidic and neutral conditions (Fig. S4).

Regarding the influence of the negative charge (Fig. 5, *C* and *C'*), we found that the peak in frequency shift increases when the percentage of PIP_2 increases from 2 to 8% and was even higher for the POPS membranes, where the peak in dissipation was also the highest for the POPS membrane in comparison to all the PIP_2 ones. Here, again, the plateau values were similar, independent of the initial charge of the PIP_2 or POPS-SUVs.

Interactions between moesin and PIP_2-SLBs followed by QCM-D

The adsorption of WT and DD moesin was then studied on the preformed PIP_2-SLBs for increasing PIP_2 concentrations and under conditions of "single microinjection" or continuous flow (Fig. 6). The same data can be plotted in two different manners, for ΔF as a function of the protein concentration for increasing PIP_2 concentrations (Fig. 6, *B* and *B'*), or for ΔF as a function of PIP_2 concentration for

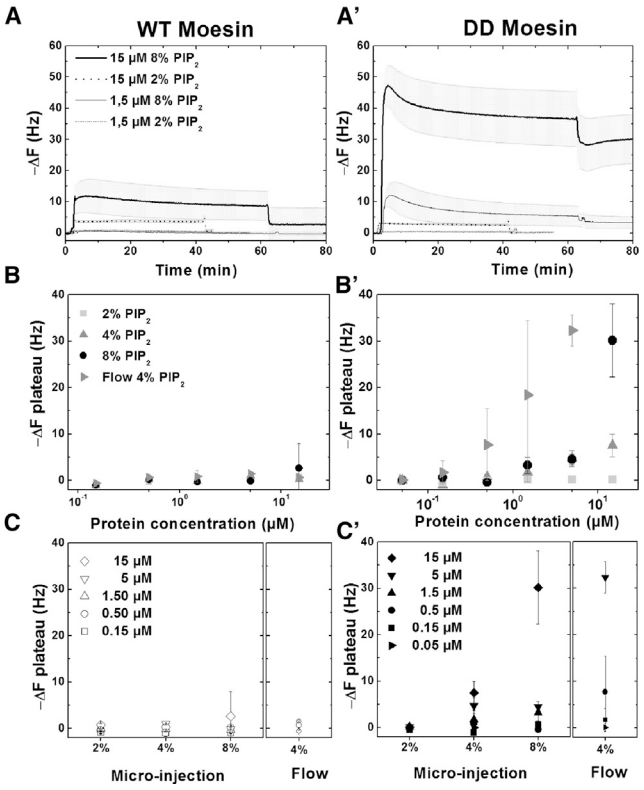

FIGURE 6 WT and DD moesin interactions with PIP_2-SLBs studied in real time by QCM-D. The proteins were either microinjected in a single injection or injected under constant flow. Representative in situ adsorption curves for WT moesin (*A*) and DD moesin (*A'*) for two different concentrations of PIP_2 (2 and 8%) and two concentrations of moesin (1.5 and 15 μM). (*B* and *B'*) The frequency shift, ΔF, at the plateau value of moesin adsorption is given for PIP_2-SLBs containing increasing concentrations of PIP_2 (2, 4, and 8%) for increasing concentrations of moesin from 0.05 to 15 μM. (*C* and *C'*) Same data of protein adsorption replotted differently, the *X* axis being now the percentage of PIP_2 in the SLB membranes. The different concentrations of WT moesin (0.15–15 μM (*C*)) and DD moesin (0.05–15 μM (*C'*)) are shown. For comparison, the ΔF values obtained in the continuous flow condition are also given for PIP_2-SLBs containing 4% PIP_2. All data in (*B*), (*B'*), (*C*), and (*C'*) show the mean ± SD of at least three independent experiments.

increasing protein concentrations (Fig. 6, *C* and *C'*). Representative adsorption kinetics are shown for microinjection of WT moesin (Fig. 6 *A*) and DD moesin (Fig. 6 *A'*) at 1.5 μM and at the highest studied protein concentration of 15 μM. First, we found that the adsorption of DD moesin was systematically higher than that of WT moesin, with a maximum frequency shift of 30.2 ± 7.9 Hz for DD moesin as compared to 2.6 ± 5.3 Hz for WT moesin with 8% PIP_2. As expected, the adsorption depended on the percentage of PIP_2 in the SLBs, a trend that was particularly visible for DD moesin. Besides, when WT and DD moesin were mixed at a given ratio, the quantity of protein bound increased with the percentage of moesin DD (Fig. S5). We observed that DD-moesin adsorption depended on the ionic strength, since adsorption was much higher at 20 mM than at 100 mM NaCl (Fig. S6). This suggests that electrostatic interactions are a major driving force.

We also noted that the adsorption was highly sensitive to the experimental conditions ("microinjection" or presence of flow (Fig. 6, *C* and *C'*)). Moesin adsorption was much higher in the case of flow than for a single microinjection, notably for DD moesin. Indeed, when recorded over several hours, a steady adsorption of DD moesin on PIP_2-SLBs was observed in the range studied, whereas that of WT moesin was fast and independent of flow (Fig. S7). Such flow-rate dependency of adsorption has previously been attributed to mass-transport limited binding (60,61) (also called diffusion-limited binding).

Having found that DD moesin adsorption on PIP_2-SLBs was dependent on protein concentration and flow, we studied the adsorption behavior of WT and DD moesin when the two proteins were adsorbed in a cumulative way at increasing concentrations on 4% PIP_2-SLBs, as compared to membranes containing 20% POPS (Fig. 7). Adsorption was followed by only a little desorption during the rinsing phases. Here again, the adsorption of DD moesin was much higher than that of WT moesin, the maximum frequency shift for WT moesin being ~10 Hz, in contrast to 55 Hz for DD moesin (Fig. 7 *A*). The dissipation also steadily increased upon adsorption of the proteins (Fig. 7 *A'*). This high dissipation, which indicates a non-dense protein layer, suggests that both WT and DD protein are in open conformation once adsorbed to the PIP2-SLBs. By plotting the plateau values in ΔF measured for increasing protein concentrations and fitting the data using Eq. 3 (Fig. 7 *B*), we deduced an apparent K_d (4.5 ± 0.7 μM, Hill coefficient $n = 2$) for DD moesin on PIP_2-SLBs. This K_d is only an estimate, since there is no desorption of the protein and thus no true equilibrium. Plotting ΔD as a function of ΔF (Fig. 7 *B'*) showed a linear relationship indicating that the adsorption of the protein is similar to that of discrete objects (51). There seemed to be no water loss but rather a restructuring of the protein on the membrane, possibly a multimerization.

DD moesin can interact with MTs

MTs have been recently found to interact with moesin both in cellulo and in vitro, but solely when their binding domain (mapped to the moesin FERM domain K211 and K212) is accessible (18). To evaluate whether the preadsorbed moesin on 4% PIP_2-SLBs can interact with MTs, we performed complementary experiments using QCM-D and TIRF (Fig. 8). MTs were injected at 5 μM in the chamber on PIP_2-membrane-preadsorbed WT and DD moesin (Fig. 8, *A* and *A'*). The preadsorbed amount of DD moesin was about twice that of WT moesin, as indicated by the initial ΔF after preadsorption of the proteins (i.e., at time close to 0). ΔF decreased during MT adsorption on DD moesin, and this decrease was irreversible after rinsing with the

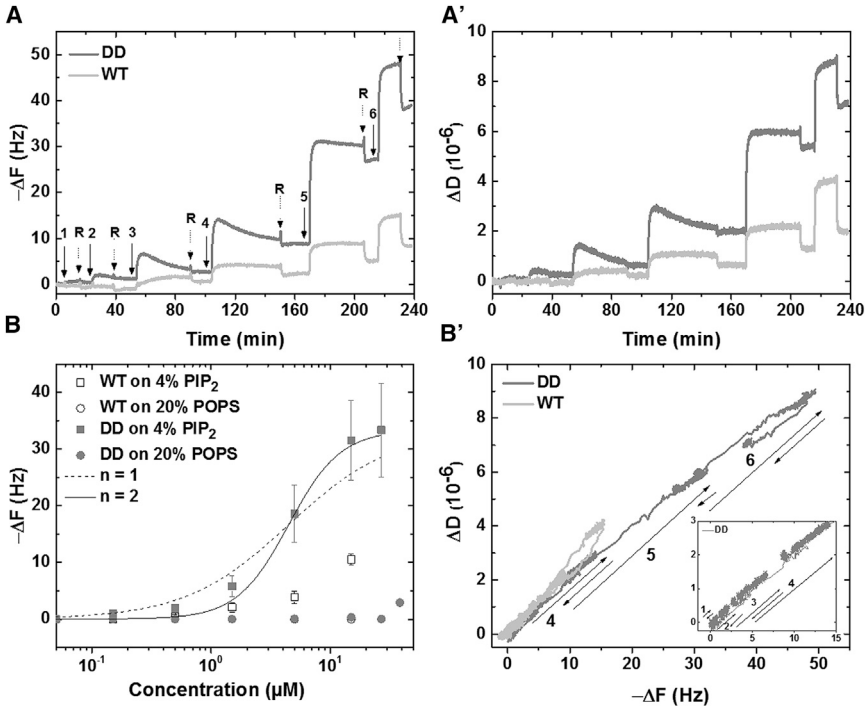

FIGURE 7 WT and DD moesin adsorption on PIP$_2$ and POPS-SLBs followed in real time by QCM-D. WT and DD moesin were adsorbed at increasing concentrations (numbers 1–6 are 0.05, 0.15, 0.5, 1.5, 5, and 15 μM, respectively) by microinjections on PIP$_2$-SLBs containing 4% PIP$_2$ and on POPS SLBs containing 20% POPS. Short rinsing is indicated by R. The kinetic curves show the steady adsorption of the proteins with a corresponding frequency shift, ΔF (*A*), and dissipation shift, ΔD (*A'*). Quantitative analysis of the QCM-D experiments by plotting ΔF as a function of the cumulative protein concentration (*B*) along with the combined time-independent DD versus DF graph (*B'*). Data are represented as the mean ± SD of at least three independent experiments. Fits to the experimental data correspond to a 1:1 interaction (*dashed line*) or a 2:1 interaction (*solid line*). The K_d value deduced from the fits is 4.5 ± 0.7 μM for DD moesin (with Hill coefficient $n = 2$).

buffer. In contrast, in the case of WT moesin, ΔF decreased only slightly and reversibly. Concomitantly, the dissipation value, *D*, irreversibly decreased solely in the case of MT adsorption on DD moesin. Imaging of MTs on preadsorbed moesin using TIRF microscopy (Fig. 8 *B*), and quantification of their fluorescence intensity (Fig. 8 *C*), confirmed that MT adsorption was higher in the case of DD moesin than for WT moesin.

DISCUSSION

Formation of PIP$_2$-containing bilayers in a calcium-free medium

The formation of SLBs containing negatively charged lipids in a calcium-free medium is known to be experimentally tricky in view of the electrostatic repulsions between the SUVs and the supporting substrate (52). For PIP$_2$-SLBs, it has been shown that forming SLBs containing >1% of PIP$_2$ is not possible at physiological pH of 7.4 (55). It is precisely for this reason that recent studies have systematically studied the effect of pH and type of buffer in the formation of PIP$_2$-SLBs, first by reflectometric interference spectroscopy and fluorescence imaging (33) and then using QCM-D and AFM (58). It was shown that PIP$_2$ can diffuse freely in the SLB (33) and that it is accessible to protein binding, notably with the ezrin FERM domain (58). Here, we demonstrate the effective formation of the PIP$_2$-SLBs when the negative charge of the PIP$_2$-SUVs is decreased (Fig. 4). Besides, PIP$_2$-SLBs containing up to 8% of PIP$_2$ could be reproducibly formed (Fig. 5), the frequency shifts and dissipation values proving the effective fusion of the PIP$_2$-SUVs.

Oligomerization state of WT versus DD moesin

In cellulo, it is accepted that the monomeric form of ERM proteins is the active form, localized at the plasma membrane, whereas the dimeric form is inactive and mostly found in the cytoplasm (19,20,26). To our knowledge, our study is the first to investigate the oligomerization state of moesin and double phosphomimetic mutant moesin in solution, since the very few published studies have always focused on ezrin (62–64). Our results (Fig. 2) show that WT-moesin contains a mixed population of monomers/dimers (~2/3:1/3, respectively), the protein oligomeric state being insensitive to PIP$_2$ in solution, whereas DD moesin is more predominantly monomeric (80–85% monomers) and forms multimers in the presence of PIP$_2$ in solution at the protein concentrations studied (2 and 8 μM). According to a recent structural study (64), ezrin dimers form in a head-to-tail manner, a process that is triggered thanks to a bistable structure of a hydrophobic core in subdomain F3. Our data (Fig. 2) showing a more elongated dimer in comparison to monomeric moesin are thus in agreement with these structural predictions. The FERM/C-ERMAD interactions are known to be sensitive to the type of buffer used in the experiments (65), which suggests that intramolecular interactions are very finely regulated.

Bretscher and co-workers (62) previously showed, using sucrose gradient sedimentation, that the EzT567D monomer

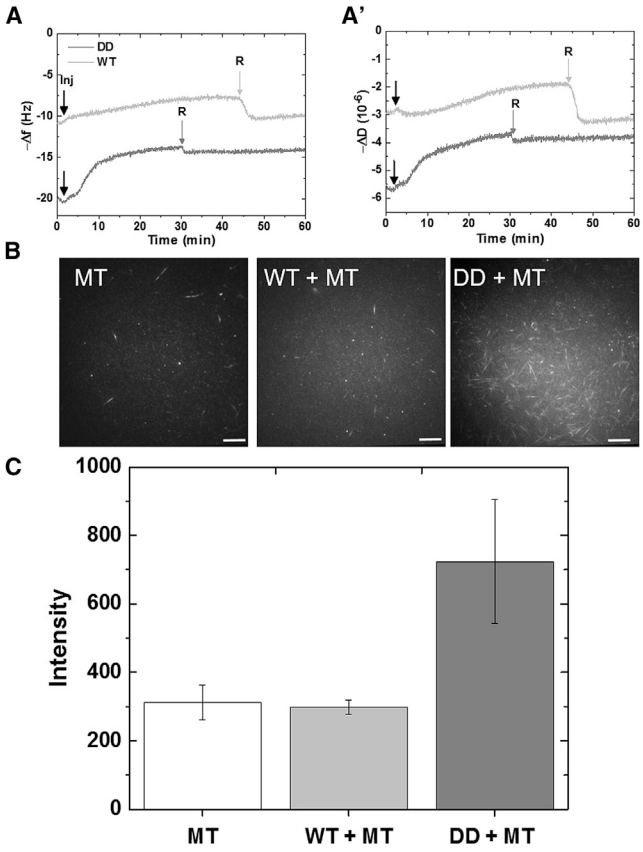

FIGURE 8 MT interactions with WT and DD moesin followed by QCM-D and TIRF microscopy. (*A* and *A'*) ΔF and ΔD, respectively, of MTs injected under constant flow at 5 μM in the chamber after preadsorption of WT and DD moesin on a 4% PIP2-containing membrane (*arrow*) and finally rinsed (*R*). (*B*) MT interactions with WT or DD moesin preadsorbed to 4% PIP_2-SLBs were imaged by TIRF microscopy. Scale bars, 20 μm. (*C*) Total mean fluorescence intensity of the image field (mean of $n = 7$ independent images).

had only a slightly increased Stokes radius. In fact, this mutant behaved very similarly to WT ezrin, the single phosphomutation having only a small effect on the FERM/C-ERMAD interactions and being unable to bind F-actin. The authors hypothesized that the differences between T567D and WT ezrin were only in the equilibrium time between the closed and open conformations. In a recent structural study using small-angle neutron scattering (SANS), Jayasundar et al. (66) showed that without PIP_2, the phosphomimetic mutants adopted essentially a closed conformation in solution similar to that observed for WT ezrin. However, after binding to a PIP_2-containing membrane, an increased fraction of the phosphomimetic ezrin mutants (T567D and S249D) was capable of binding to proteins (such as NHERF1), as compared to WT ezrin, and was also able to bind to F-actin. Their results agreed with those of Bretscher (62): the phosphomimetic mutants are more dynamic, so that a small fraction of the mutants is in the "open" conformation for a long enough time period to be competent to bind to other proteins. In addition, our previous results using DLS and Western blots (63) showed that PIP_2 specifically induced a conformational change in full-length ezrin and the formation of oligomers.

Scattering techniques, such as small-angle x-ray scattering (SAXS) and SANS, may be useful to gain insight into the structure of WT and mutant moesin in solution. SAXS is more and more used (67,68) but requires access to synchrotron radiation, which could not be achieved in the timeframe of our study. SANS requires the sample to be deuterated to get contrast using neutrons. To our knowledge, neither SAXS nor SANS has been used on WT and mutant moesin but they were recently used to study ezrin monomer versus dimer structures (64) as well as the role of a phosphomimetic mutation in ezrin (66). In the latter study, the authors did not detect any difference between the monomer and dimer by SAXS. Using SAXS yielded no difference between the different WT ezrin and mutant ($R_g = 4.1$ nm and $D_{max} = 14$ nm), but PIP_2 induced a conformational change with $R_g = 6.2$ nm and $D_{max} = 24$ nm (66). In contrast, using SAXS, Curmi and colleagues (64) found an increased radius of gyration and length for the dimer in comparison to the ezrin monomer ($R_g = 9.5 \pm 0.5$ nm vs. $R_g = 4 \pm 0.1$ nm; $D_{max} = 32.5 \pm 0.05$ vs. 6.5 ± 0.5 nm). They proposed a model with two FERM/C-terminal domain complexes at opposite ends of the central coiled coil producing a dumbbell-shaped molecule.

Thus, the findings presented here highlight a different behavior of moesin versus ezrin in their sensitivity to and interaction with PIP_2 in solution and in biomimetic membranes. We proved that DD moesin has a better affinity to PIP_2 in biomimetic membranes and that, presumably, the double phosphomimetic mutation changes the structure of the FERM domain and enables the cooperative interaction of DD moesin with PIP_2-LUVs (Fig. 3) as well as PIP_2-SLBs (Figs. 6 and 7). Clearly, electrostatic interactions are also coming into play, since decreasing ionic strength increases the binding of DD moesin to PIP_2-LUVs (Fig. S6).

DD moesin can interact via the two PIP_2-binding sites, patch and pocket

ERM interactions with PIP_2 at the plasma membrane have already been shown to involve a PIP_2-binding site (22) and to rely on a previous phosphorylation step (in ezrin T567D). Phosphorylation contributes to the opening of the molecule by unfolding of the central α-helical domain (69) for subsequent binding of the FERM domain to the plasma membrane (19) and interaction with actin filaments. Structural analysis of the radixin FERM domain has also identified a PIP_2-binding pocket (24), which is masked initially in the closed conformation but can be unmasked after binding to the "basic" patch, localized at the external part of the FERM domain on the positive part of the F3 lobe (26). In addition, recent experiments on moesin and PIP_2-LUVs (26) have proven that moesin is binding

sequentially to the membrane, first via the patch (corresponding to K253/K254 and K262/K263 residues), which leads first to a conformational change of an acidic linker domain followed by the binding of the pocket (K63, K278). These authors showed that the patch is essential for all three functions in membrane localization of moesin, moesin binding to PIP_2, and PIP_2-induced release of moesin autoinhibition.

Here, our results show that the double phosphomimetic mutant, DD moesin, has an increased interaction with both PIP_2-LUVs (Fig. 3) and PIP_2-SLBs (Figs. 6 and 7). This interaction is cooperative for DD moesin and PIP_2 (Hill coefficient $n = 2.4$ for PIP_2-LUVs) as well as for incoming moesin molecules with two preadsorbed proteins ($n = 2$ for SLBs) but solely in the case of DD, and not WT, moesin. In addition, DD moesin tends to be essentially monomeric in solution (10–20 wt % of dimers) and is sensitive to micellar PIP_2 (Fig. 2), whereas 30% of WT moesin forms dimers in solution (Fig. 2), the protein being almost insensitive to PIP_2. Finally, the interaction of DD moesin with PIP_2-SLBs is sensitive to flow at the studied concentrations, whereas that of WT moesin is not (Figs. 6 and S7). This flow sensitivity may be explained by the shear force driving clustering at the interface with the PIP2-SLBs, allowing more protein to bind.

Altogether, our results support the conclusion that the phosphomimetic mutation changes both the intramolecular interactions within the FERM domain and the interactions with PIP_2-containing membranes. Our results are in agreement with the presence of two available binding sides in DD moesin, which may correspond to the "patch" and the "pocket." This reinforced binding leads to more stable DD moesin/PIP_2-SLB interactions (Fig. 7), which are indeed resistant to flow (Fig. 6). From the kinetics data and the presence of an initial overshoot in the adsorption curve (Fig. 6 *A'*), we can hypothesize that binding is sequential, with a first interaction followed by a conformational rearrangement so that the protein can reinforce binding. In contrast, WT moesin barely interacts with PIP_2-SLBs, and this interaction is not improved by the presence of flow at the concentration analyzed (Fig. 6, *B* and *C*). However, for both WT and DD moesin, binding is history dependent, meaning that preadsorbed WT or DD moesin molecules facilitate the adsorption of incoming proteins on the membrane. This indicates that protein-protein interactions are likely to drive adsorption, either laterally or via their C-terminal domains, which reinforces the initial electrostatic interactions with the negatively charged membrane. Indeed, the overshoot, which we attribute to the reorganization of the DD moesin on the PIP_2-SLBs and subsequent lateral protein-protein association, is not present for WT moesin. Together with the fact that the high dissipation value measured by QCM-D is indicative of an open conformation for WT and DD moesin adsorbed to PIP_2-SLBs (Fig. 7 *A'*),

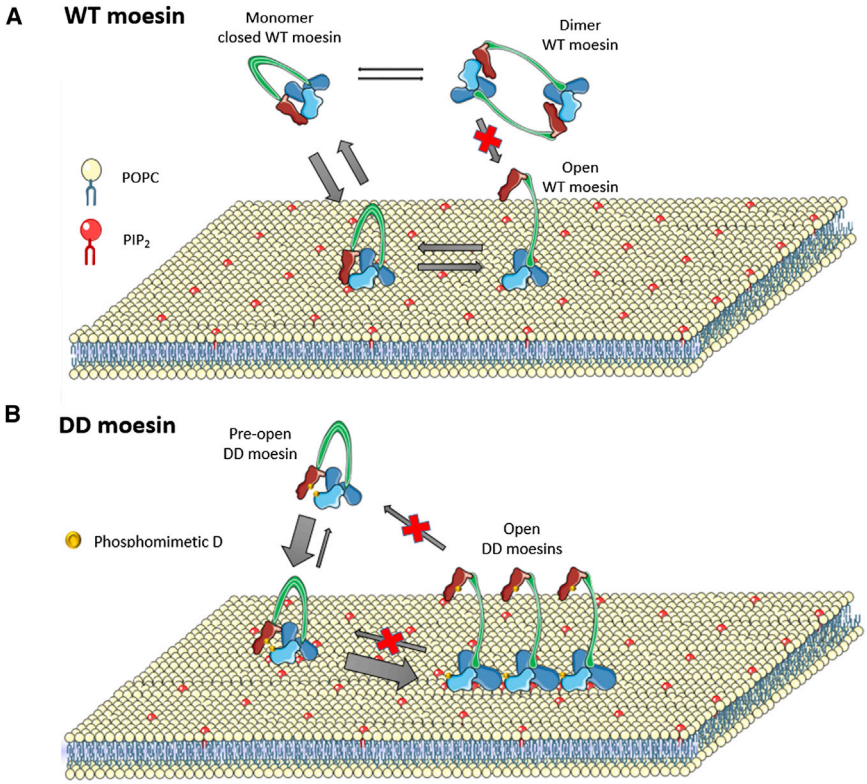

FIGURE 9 Proposed model of WT and DD moesin adsorption on PIP_2-SLBs. (*A*) For WT moesin, the dimeric form barely interacts with PIP_2 in SLBs, since the FERM/C-ERMAD are in a head-to-tail orientation. The protein in the monomeric form is in a closed conformation, which slightly but not fully opens upon PIP_2 interaction with PIP_2-SLBs (*A*). In contrast, the conformation of DD moesin (*B*) is more open, which enables its interactions with PIP_2-SLBs and subsequent reorganization to bind two PIP_2 molecules. This reinforces the interactions, which are mostly irreversible and involve several lateral protein-protein interactions (*B*). To see this figure in color, go online.

TABLE 1 Comparison between Ezrin and Moesin with Respect to Their Interactions with Different Biomimetic Membranes

Biomimetic Membrane	ERM Protein			
	Ezrin WT	Ezrin T567D	Moesin WT	Moesin T235D, T567D
LUVs	1:1 interaction, K_d similar to that of moesin (28,29)	–	1: 1 interaction, K_d similar to that of ezrin ((29) and this study)	cooperativity and lower K_d (this study)
GUVs	cooperativity (30)	–	–	–
SLBs	cooperativity and irreversible binding (34,70)	less multimers and irreversible binding (34,35)	noncooperative and reversible binding (this study)	cooperativity and irreversible binding (this study)

Comparison between Ezrin and Moesin with respect to their interactions with different biomimetic membranes. The model membranes studied were LUVs, GUVs and SLBs. For ezrin, only the single phosphomimetic mutation has been studied.

the irreversible interaction of MT with DD moesin preadsorbed on PIP_2-SLBs further supports the idea that DD moesin is in an open conformation once adsorbed on the PIP_2-SLBs.

We propose the following model to explain WT and DD moesin interactions with PIP_2-containing membranes (Fig. 9). For WT moesin (Fig. 9 *A*), the dimeric form barely interacts with PIP_2 in SLBs, since the FERM/C-ERMAD are in a head-to-tail conformation (64). The protein in the monomeric form is in a closed conformation, which is slightly but not fully open upon PIP_2 interaction with PIP_2-SLBs. In contrast, the conformation of DD moesin is more open, which enables its interactions with PIP_2-SLBs and subsequent reorganization to bind two PIP_2 molecules. This reinforces the interactions, which are mostly irreversible and involve lateral protein-protein interactions.

Ezrin and moesin exhibit distinct behaviors in their interactions with PIP_2 biomimetic membranes of different curvature

As mentioned above, previous studies from the literature and the results presented here point to a different behavior of moesin and ezrin in their interactions with PIP_2-containing membranes. Ezrin appears to be sensitive to curvature, its interactions being cooperative when planar PIP_2-membranes are used, such as PIP_2-SLBs (70) and PIP_2-GUVs (30) but not cooperative in the case of PIP_2-LUVs (28,29). A single phosphomimetic mutation on ezrin (T567D) only slightly increases its binding to F-actin. It is only the combination of PIP_2 binding and phosphomutation that enables ezrin to be in a fully activated state (35).

In contrast, whereas WT moesin is sensitive to curvature (higher binding with PIP_2-LUVs (Fig. 3) than with PIP_2-SLBs (Fig. 7)), DD moesin is insensitive to membrane curvature. In the case of moesin, the double phosphomimetic mutant is able to induce a cooperative adsorption via two PIP_2-binding sites. The differences for ezrin, moesin and their phosphomimetic mutants in binding to PIP_2-containing membranes are summarized in Table 1.

Altogether, our results suggest that DD moesin is in a more open conformation than WT moesin and interacts in a cooperative manner with PIP_2-LUVs as well as PIP_2-SLBs. These interactions are presumably based on two major binding sites, the "patch" and the "pocket," whose roles have recently been studied in cellulo in lymphocytes (26). Higher binding is reinforced by a liquid flow as well as by preadsorbed moesin molecules. Our results show that both phosphorylation and interactions with PIP_2 mutually contribute to the opening of moesin and to its linkage between the plasma membrane and the cell cytoskeleton.

SUPPORTING MATERIAL

Seven figures are available at http://www.biophysj.org/biophysj/supplemental/S0006-3495(17)31202-X.

AUTHOR CONTRIBUTIONS

C.P. conceived and coordinated the study. All authors contributed to designing the research and analyzing the data. Q.L. carried out LUV and SLB preparation and protein/membrane interactions with the help of H.V. and M.K. Q.L., F.D., H.V., and M.L. produced the recombinant proteins. M.W. and M.L. worked on the structural representation. A.L.R. and C.E. carried out AUC experiments and helped in their analysis. C.P., Q.L., and M.W. wrote the article. All authors read and commented on the manuscript.

ACKNOWLEDGMENTS

The authors thank Christian Roy and Daniele Gulino for fruitful discussions and technical suggestions. The authors thank Cyril Favard, Dhruv Thakar, Liliane Guerente, and Ralf Richter for fruitful discussions regarding the QCM-D experiments and Hugues Bonnet for his technical help. The authors also acknowledge scientific or technical support from the chemistry platform "NanoBio campus" in Grenoble, where this work was performed. We acknowledge the support of Luca Signor for mass spectroscopy experiments analysis. Experiments with tubulin were done with the help of Laurent Blanchoin and Jérémie Gaillart from CEA/BIG in Grenoble.

This work was supported by the European Commission (FP7 program) via an European Research Council Starting Grant 2010 (GA259370) to C.P. and by an Agence National de la Recherche grant (ANR-13-BSV5-0006-02 Fluobuds). C.P. is a Senior Member of the Institut Universitaire de France, whose support is gratefully acknowledged. This work also used the

"Plateau Caractérisation des Interactions" (PCI) from the Institute de Chimie Moléculaire de Grenoble (ICMG) and the platforms of the Grenoble Instruct Center (ISBG; UMS 3518 CNRS-CEA-UJF-EMBL) with support from the Infrastructure Française Pour La Biologie Structurale Integree (ANR-10-INSB-05-02) and the Grenoble Alliance for Structural Biology (ANR-10-LABX-49-01) within the Grenoble Partnership for Structural Biology (PSB).

REFERENCES

1. Fehon, R. G., A. I. McClatchey, and A. Bretscher. 2010. Organizing the cell cortex: the role of ERM proteins. *Nat. Rev. Mol. Cell Biol.* 11:276–287.
2. Niggli, V., and J. Rossy. 2008. Ezrin/radixin/moesin: versatile controllers of signaling molecules and of the cortical cytoskeleton. *Int. J. Biochem. Cell Biol.* 40:344–349.
3. Hao, J. J., Y. Liu, …, S. Shaw. 2009. Phospholipase C-mediated hydrolysis of PIP_2 releases ERM proteins from lymphocyte membrane. *J. Cell Biol.* 184:451–462.
4. Shaffer, M. H., R. S. Dupree, …, J. K. Burkhardt. 2009. Ezrin and moesin function together to promote T cell activation. *J. Immunol.* 182:1021–1032.
5. Hirata, T., A. Nomachi, …, S. Narumiya. 2012. Moesin-deficient mice reveal a non-redundant role for moesin in lymphocyte homeostasis. *Int. Immunol.* 24:705–717.
6. Matsumoto, M., and T. Hirata. 2016. Moesin regulates neutrophil rolling velocity in vivo. *Cell. Immunol.* 304-305:59–62.
7. Parameswaran, N., and N. Gupta. 2013. Re-defining ERM function in lymphocyte activation and migration. *Immunol. Rev.* 256:63–79.
8. Liu, Y., N. V. Belkina, and S. Shaw. 2009. HIV infection of T cells: actin-in and actin-out. *Sci. Signal.* 2:pe23.
9. Barrero-Villar, M., J. R. Cabrero, …, A. Valenzuela-Fernández. 2009. Moesin is required for HIV-1-induced CD4-CXCR4 interaction, F-actin redistribution, membrane fusion and viral infection in lymphocytes. *J. Cell Sci.* 122:103–113.
10. Kubo, Y., H. Yoshii, …, N. Yamamoto. 2008. Ezrin, Radixin, and Moesin (ERM) proteins function as pleiotropic regulators of human immunodeficiency virus type 1 infection. *Virology.* 375:130–140.
11. Giretti, M. S., M. M. Montt Guevara, …, T. Simoncini. 2014. Effects of estetrol on migration and invasion in T47-D breast cancer cells through the actin cytoskeleton. *Front. Endocrinol. (Lausanne).* 5:80.
12. Estecha, A., L. Sánchez-Martín, …, P. Sánchez-Mateos. 2009. Moesin orchestrates cortical polarity of melanoma tumour cells to initiate 3D invasion. *J. Cell Sci.* 122:3492–3501.
13. Beaty, B. T., and J. Condeelis. 2014. Digging a little deeper: the stages of invadopodium formation and maturation. *Eur. J. Cell Biol.* 93:438–444.
14. Adada, M., D. Canals, …, L. M. Obeid. 2014. Sphingolipid regulation of ezrin, radixin, and moesin proteins family: implications for cell dynamics. *Biochim. Biophys. Acta.* 1841:727–737.
15. Ilani, T., C. Khanna, …, A. Bretscher. 2007. Immune synapse formation requires ZAP-70 recruitment by ezrin and CD43 removal by moesin. *J. Cell Biol.* 179:733–746.
16. Yang, H. S., and P. W. Hinds. 2003. Increased ezrin expression and activation by CDK5 coincident with acquisition of the senescent phenotype. *Mol. Cell.* 11:1163–1176.
17. Viswanatha, R., J. Wayt, …, A. Bretscher. 2013. Interactome analysis reveals ezrin can adopt multiple conformational states. *J. Biol. Chem.* 288:35437–35451.
18. Solinet, S., K. Mahmud, …, S. Carreno. 2013. The actin-binding ERM protein Moesin binds to and stabilizes microtubules at the cell cortex. *J. Cell Biol.* 202:251–260.
19. Gautreau, A., D. Louvard, and M. Arpin. 2000. Morphogenic effects of ezrin require a phosphorylation-induced transition from oligomers to monomers at the plasma membrane. *J. Cell Biol.* 150:193–203.
20. Zhu, L., Y. Liu, and J. G. Forte. 2005. Ezrin oligomers are the membrane-bound dormant form in gastric parietal cells. *Am. J. Physiol. Cell Physiol.* 288:C1242–C1254.
21. Pearson, M. A., D. Reczek, …, P. A. Karplus. 2000. Structure of the ERM protein moesin reveals the FERM domain fold masked by an extended actin binding tail domain. *Cell.* 101:259–270.
22. Barret, C., C. Roy, …, V. Niggli. 2000. Mutagenesis of the phosphatidylinositol 4,5-bisphosphate (PIP(2)) binding site in the NH_2-terminal domain of ezrin correlates with its altered cellular distribution. *J. Cell Biol.* 151:1067–1080.
23. Fievet, B. T., A. Gautreau, …, M. Arpin. 2004. Phosphoinositide binding and phosphorylation act sequentially in the activation mechanism of ezrin. *J. Cell Biol.* 164:653–659.
24. Hamada, K., T. Shimizu, …, T. Hakoshima. 2000. Structural basis of the membrane-targeting and unmasking mechanisms of the radixin FERM domain. *EMBO J.* 19:4449–4462.
25. Hirao, M., N. Sato, …, S. Tsukita. 1996. Regulation mechanism of ERM (ezrin/radixin/moesin) protein/plasma membrane association: possible involvement of phosphatidylinositol turnover and Rho-dependent signaling pathway. *J. Cell Biol.* 135:37–51.
26. Ben-Aissa, K., G. Patino-Lopez, …, S. Shaw. 2012. Activation of moesin, a protein that links actin cytoskeleton to the plasma membrane, occurs by phosphatidylinositol 4,5-bisphosphate (PIP_2) binding sequentially to two sites and releasing an autoinhibitory linker. *J. Biol. Chem.* 287:16311–16323.
27. Maniti, O., K. Carvalho, and C. Picart. 2013. Model membranes to shed light on the biochemical and physical properties of ezrin/radixin/moesin. *Biochimie.* 95:3–11.
28. Blin, G., E. Margeat, …, C. Picart. 2008. Quantitative analysis of the binding of ezrin to large unilamellar vesicles containing phosphatidylinositol 4,5 bisphosphate. *Biophys. J.* 94:1021–1033.
29. Maniti, O., N. Khalifat, …, C. Picart. 2012. Binding of moesin and ezrin to membranes containing phosphatidylinositol (4,5) bisphosphate: a comparative study of the affinity constants and conformational changes. *Biochim. Biophys. Acta.* 1818:2839–2849.
30. Carvalho, K., L. Ramos, …, C. Picart. 2008. Giant unilamellar vesicles containing phosphatidylinositol(4,5)bisphosphate: characterization and functionality. *Biophys. J.* 95:4348–4360.
31. Takeda, S., A. Saitoh, …, K. Takiguchi. 2006. Opening of holes in liposomal membranes is induced by proteins possessing the FERM domain. *J. Mol. Biol.* 362:403–413.
32. Janke, M., A. Herrig, …, A. Janshoff. 2008. Actin binding of ezrin is activated by specific recognition of PIP_2-functionalized lipid bilayers. *Biochemistry.* 47:3762–3769.
33. Braunger, J. A., C. Kramer, …, C. Steinem. 2013. Solid supported membranes doped with PIP_2: influence of ionic strength and pH on bilayer formation and membrane organization. *Langmuir.* 29:14204–14213.
34. Bosk, S., J. A. Braunger, …, C. Steinem. 2011. Activation of F-actin binding capacity of ezrin: synergism of PIP_2 interaction and phosphorylation. *Biophys. J.* 100:1708–1717.
35. Shabardina, V., C. Kramer, …, C. Steinem. 2016. Mode of ezrin-membrane interaction as a function of PIP_2 binding and pseudophosphorylation. *Biophys. J.* 110:2710–2719.
36. Aumeier, C., L. Schaedel, …, M. Théry. 2016. Self-repair promotes microtubule rescue. *Nat. Cell Biol.* 18:1054–1064.
37. Arnal, I., and R. H. Wade. 1995. How does taxol stabilize microtubules? *Curr. Biol.* 5:900–908.
38. Moens, P. D. J., and L. a. Bagatolli. 2007. Profilin binding to submicellar concentrations of phosphatidylinositol (4,5) bisphosphate and phosphatidylinositol (3,4,5) trisphosphate. *Biochim. Biophys. Acta.* 1768:439–449.

39. Schuck, P. 2000. Size-distribution analysis of macromolecules by sedimentation velocity ultracentrifugation and Lamm equation modeling. *Biophys. J.* 78:1606–1619.

40. Hunter, R. J. 1981. Zeta Potential in Colloid Science. Academic Press, New York.

41. Saarikangas, J., H. Zhao, and P. Lappalainen. 2010. Regulation of the actin cytoskeleton-plasma membrane interplay by phosphoinositides. *Physiol. Rev.* 90:259–289.

42. Yonemura, S., T. Matsui, …, S. Tsukita. 2002. Rho-dependent and -independent activation mechanisms of ezrin/radixin/moesin proteins: an essential role for polyphosphoinositides in vivo. *J. Cell Sci.* 115:2569–2580.

43. Mani, T., R. F. Hennigan, …, W. Ip. 2011. FERM domain phosphoinositide binding targets merlin to the membrane and is essential for its growth-suppressive function. *Mol. Cell. Biol.* 31:1983–1996.

44. Sutkeviciute, I., M. Thépaut, …, F. Fieschi. 2014. Unique DC-SIGN clustering activity of a small glycomimetic: a lesson for ligand design. *ACS Chem. Biol.* 9:1377–1385.

45. Schuck, P. 1998. Sedimentation analysis of noninteracting and self-associating solutes using numerical solutions to the Lamm equation. *Biophys. J.* 75:1503–1512.

46. McLaughlin, S. 1989. The electrostatic properties of membranes. *Annu. Rev. Biophys. Biophys. Chem.* 18:113–136.

47. Jurkiewicz, P., L. Cwiklik, …, M. Hof. 2012. Structure, dynamics, and hydration of POPC/POPS bilayers suspended in NaCl, KCl, and CsCl solutions. *Biochim. Biophys. Acta.* 1818:609–616.

48. Toner, M., G. Vaio, …, S. McLaughlin. 1988. Adsorption of cations to phosphatidylinositol 4,5-bisphosphate. *Biochemistry.* 27:7435–7443.

49. Sugiura, Y. 1981. Structure of molecular aggregates of 1-(3-*sn*-phosphatidyl)-L-*myo*-inositol 3,4-bis(phosphate) in water. *Biochim. Biophys. Acta.* 641:148–159.

50. Pan, J., X. Cheng, …, J. Katsaras. 2014. The molecular structure of a phosphatidylserine bilayer determined by scattering and molecular dynamics simulations. *Soft Matter.* 10:3716–3725.

51. Reviakine, I., D. Johannsmann, and R. P. Richter. 2011. Hearing what you cannot see and visualizing what you hear: interpreting quartz crystal microbalance data from solvated interfaces. *Anal. Chem.* 83:8838–8848.

52. Richter, R. P., R. Bérat, and A. R. Brisson. 2006. Formation of solid-supported lipid bilayers: an integrated view. *Langmuir.* 22:3497–3505.

53. Richter, R., A. Mukhopadhyay, and A. Brisson. 2003. Pathways of lipid vesicle deposition on solid surfaces: a combined QCM-D and AFM study. *Biophys. J.* 85:3035–3047.

54. Satriano, C., S. Svedhem, and B. Kasemo. 2012. Well-defined lipid interfaces for protein adsorption studies. *Phys. Chem. Chem. Phys.* 14:16695–16698.

55. Baumann, M. K., E. Amstad, …, E. Reimhult. 2010. Characterization of supported lipid bilayers incorporating the phosphoinositides phosphatidylinositol 4,5-biphosphate and phosphoinositol-3,4,5-triphosphate by complementary techniques. *Biointerphases.* 5:114–119.

56. Sarmento, M. J., A. Coutinho, …, F. Fernandes. 2014. Ca^{2+} induces $PI(4,5)P_2$ clusters on lipid bilayers at physiological $PI(4,5)P_2$ and Ca^{2+} concentrations. *Biochim. Biophys. Acta.* 1838:822–830.

57. Wang, Y.-H., A. Collins, …, P. A. Janmey. 2012. Divalent cation-induced cluster formation by polyphosphoinositides in model membranes. *J. Am. Chem. Soc.* 134:3387–3395.

58. Drücker, P., D. Grill, …, H.-J. Galla. 2014. Formation and characterization of supported lipid bilayers containing phosphatidylinositol-4,5-bisphosphate and cholesterol as functional surfaces. *Langmuir.* 30:14877–14886.

59. Cho, N.-J., C. W. Frank, …, F. Höök. 2010. Quartz crystal microbalance with dissipation monitoring of supported lipid bilayers on various substrates. *Nat. Protoc.* 5:1096–1106.

60. van der Meulen, S. A. J., G. V. Dubacheva, …, M. E. Leunissen. 2014. Quartz crystal microbalance with dissipation monitoring and spectroscopic ellipsometry measurements of the phospholipid bilayer anchoring stability and kinetics of hydrophobically modified DNA oligonucleotides. *Langmuir.* 30:6525–6533.

61. Schuck, P., and H. Zhao. 2010. The role of mass transport limitation and surface heterogeneity in the biophysical characterization of macromolecular binding processes by SPR biosensing. *Methods Mol. Biol.* 627:15–54.

62. Chambers, D. N., and A. Bretscher. 2005. Ezrin mutants affecting dimerization and activation. *Biochemistry.* 44:3926–3932.

63. Carvalho, K., N. Khalifat, …, L. Ramos. 2010. Phosphatidylinositol 4,5-bisphosphate-induced conformational change of ezrin and formation of ezrin oligomers. *Biochemistry.* 49:9318–9327.

64. Phang, J. M., S. J. Harrop, …, P. M. Curmi. 2016. Structural characterization suggests models for monomeric and dimeric forms of full-length ezrin. *Biochem. J.* 473:2763–2782.

65. Jayaraman, B., and L. K. Nicholson. 2007. Thermodynamic dissection of the Ezrin FERM/CERMAD interface. *Biochemistry.* 46:12174–12189.

66. Jayasundar, J. J., J. H. Ju, …, Z. Bu. 2012. Open conformation of ezrin bound to phosphatidylinositol 4,5-bisphosphate and to F-actin revealed by neutron scattering. *J. Biol. Chem.* 287:37119–37133.

67. Chaudhuri, B. N. 2015. Emerging applications of small angle solution scattering in structural biology. *Protein Sci.* 24:267–276.

68. Skou, S., R. E. Gillilan, and N. Ando. 2016. Synchrotron-based small-angle x-ray scattering (SAXS) of proteins in solution. *Nat. Protoc.* 28:1304–1314.

69. Li, Q., M. R. Nance, …, J. J. G. Tesmer. 2007. Self-masking in an intact ERM-merlin protein: an active role for the central α-helical domain. *J. Mol. Biol.* 365:1446–1459.

70. Herrig, A., M. Janke, …, C. Steinem. 2006. Cooperative adsorption of ezrin on PIP_2-containing membranes. *Biochemistry.* 45:13025–13034.

Biophysical Journal, Volume *114*

Supplemental Information

Role of Phosphorylation in Moesin Interactions with PIP_2-Containing Biomimetic Membranes

Quentin Lubart, Helene Vitet, Fabien Dalonneau, Aline Le Roy, Mathieu Kowalski, Morgane Lourdin, Christine Ebel, Marianne Weidenhaupt, and Catherine Picart

LUBART et al, Supplemental data file

Materials and Methods

Mass spectrometry

Liquid Chromatography Electrospray Ionization Mass Spectrometry (LC/ESI-MS) was applied for quality control of the intact proteins WT moesin and DD moesin by using a 6210 LC/ESI-TOF mass spectrometer interfaced with an HPLC pump system (Agilent Technologies). MS acquisition was carried out in the positive ion mode with spectra in the profile mode. The MS instrument was operated with the following experimental settings: ESI source temperature was set at 300 °C; nitrogen was used as drying gas (7 l/min) and as nebulizer gas (10 psi); the capillary needle voltage was set at 4000 V. Spectra acquisition rate was of 1.03 spectra/s. All solvents used were HPLC grade (Chromasolv, Sigma-Aldrich), trifluoroacetic acid (TFA) was from Acros Organics (puriss., p.a.). Solvent A was 0.03% TFA in water, solvent B was 95% acetonitrile-5% water-0.03% TFA. The MS spectra were acquired and the data processed with MassHunter workstation software (v. B.02.00, Agilent Technologies) and with GPMAW software (v. 7.00b2, Lighthouse Data, Denmark). The mass spectrometer was calibrated in the *m/z* 300-3000 range with standard calibrants (ESI-L, Low concentration tuning mix, Agilent Technologies) before measurements. Just before analysis the protein samples were diluted in acidic denaturing conditions to a final concentration of 5 µM with solution A (0.03% TFA in water). Samples were thermostated at 10°C in the autosampler and the analysis was run by injecting 4 µL of each sample. They were first trapped and desalted on a reverse phase-C8 cartridge (Zorbax 300SB-C8, 5um, 300µm ID×5mm, Agilent Technologies) for 3 minutes at a flow rate of 50 ul/min with 100% solvent A and then eluted with 70% solvent B at a flow rate of 50 ul/min for MS detection. The RP-C8 cartridge was then re-equilibrated for 4 min with 100% solvent A at a flow rate of 50 ul/min. Mass spectra were recorded in the 300-3000 mass-to-charge (*m/z*) range.

Spectroscopic measurement of intrinsic fluorescence of tryptophan

Tryptophan fluorescence emission spectra of WT moesin and DD moesin at 0.4 µM were recorded in the absence or after addition of increasing amounts of PIP_2-LUVs (corresponding respectively to 1, 1.7, 2.3, 2.9

mg/ml of total lipids) using a TECAN infinite 1000 fluorescence spectrometer (TECAN, Switzerland). For intrinsic fluorescence, a Hellma 96 quartz 96-well plate was used and the excitation and emission wavelength were set, respectively, to 280 $\pm$ 5 nm and 333 $\pm$ 5 nm). The measurements were made after 45 minutes of incubation in the dark, each spectrum being the average of at least 9 independent measurements. The percentage of quenching was calculated by the following equation:

$$\% \text{ of quenching} = [(Fluo_{moesin} - Fluo_{moesin+LUVs}) / Fluo_{moesin}] * 100 \quad (3)$$

Where Fluo is the fluorescence intensity (in arbitrary units)

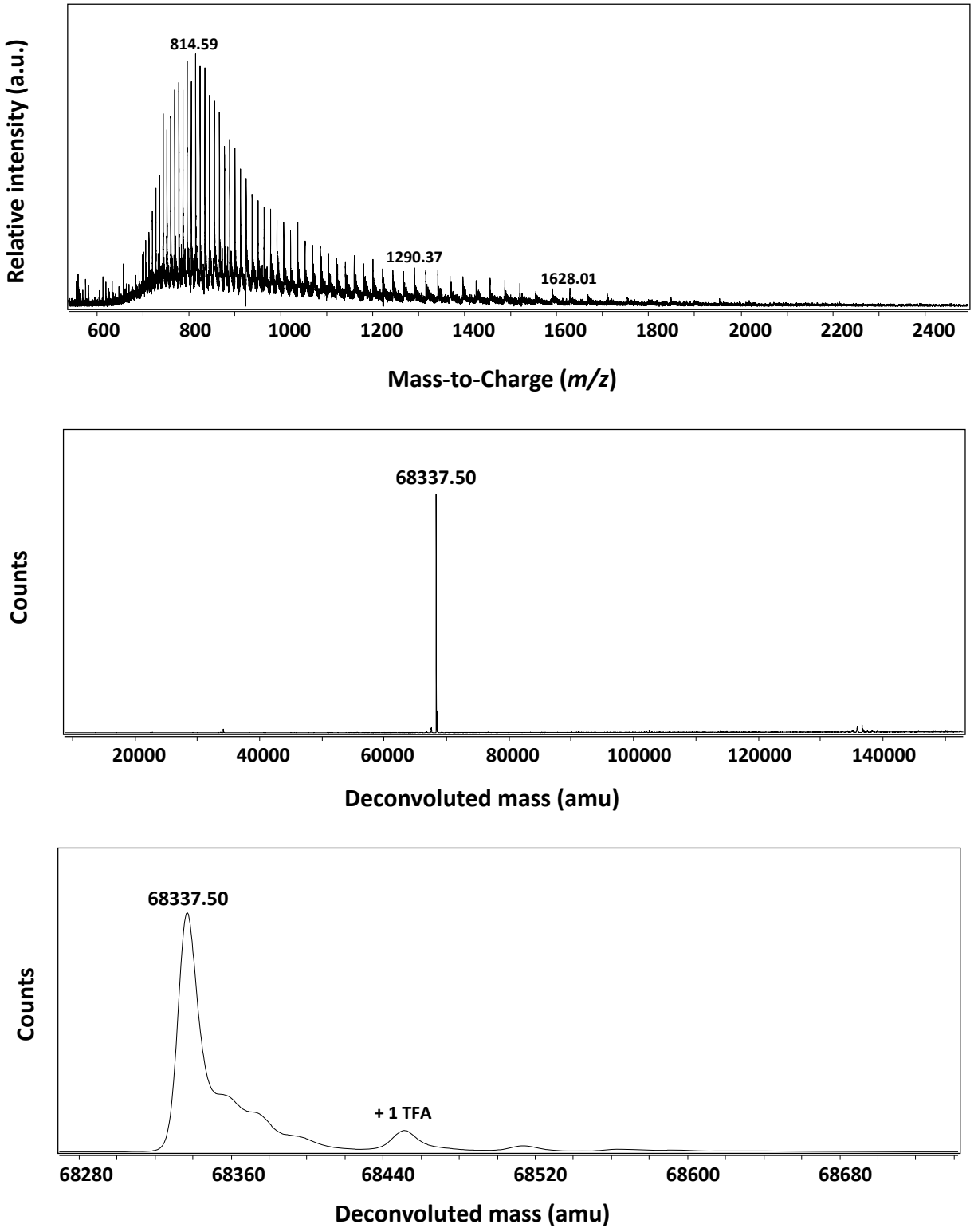

FIGURE S1. Mass spectrometry analysis of recombinant WT-moesin.

(Observed mass : 68337.50 Da, theoretical mass : 68337.71 Da, mass accuracy : 3 ppm).

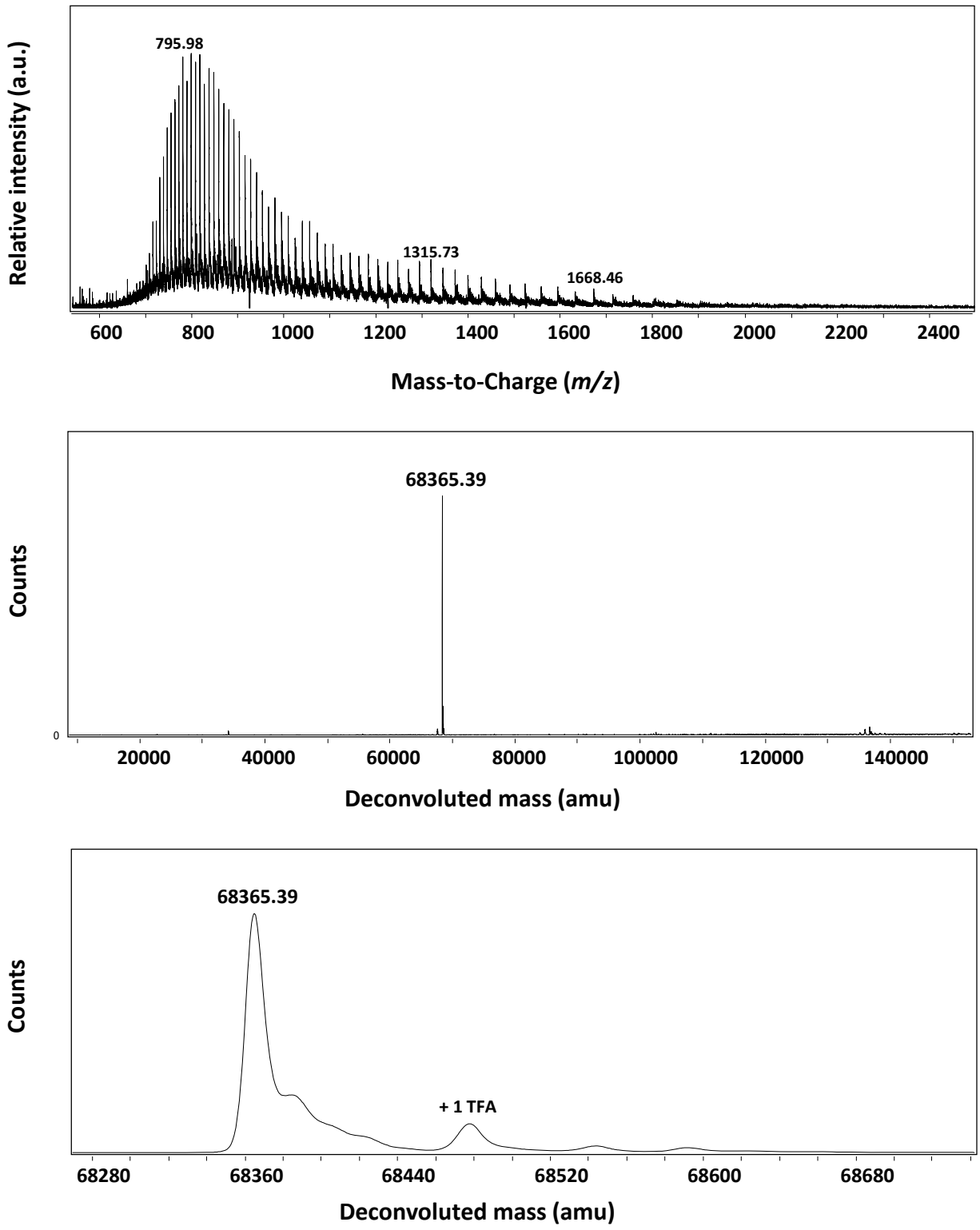

FIGURE S2. Mass spectrometry analysis of recombinant DD-moesin.

(Observed mass : 68365.39 Da, theoretical mass : 68365.67 Da, mass accuracy : 11 ppm).

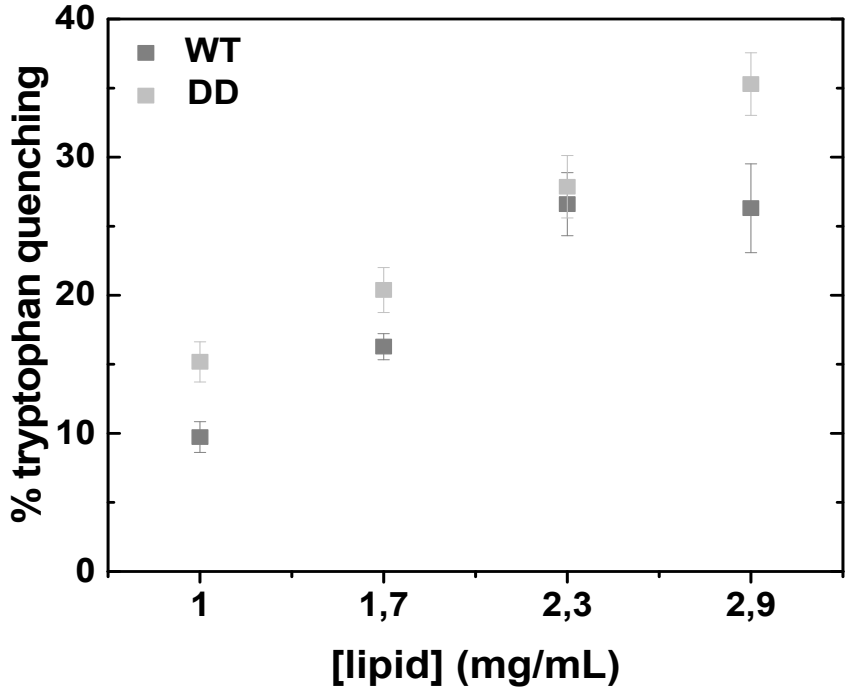

FIGURE S3. Quenching of intrinsic fluorescence of tryptophan. Quenching was measured for WT and DD-moesin as a function of the initial PIP_2-LUV concentration in solution :5% PIP_2-LUVs, 1 mg/ml = 22.8 µM $[PIP_2]_{acc}$; 1.7 mg/ml = 38.7µM $[PIP_2]_{acc}$; 2.3 mg/ml = 52.5 µM $[PIP_2]_{acc}$ and 2.9 mg/ml = 66.1 µM $[PIP_2]_{acc}$.

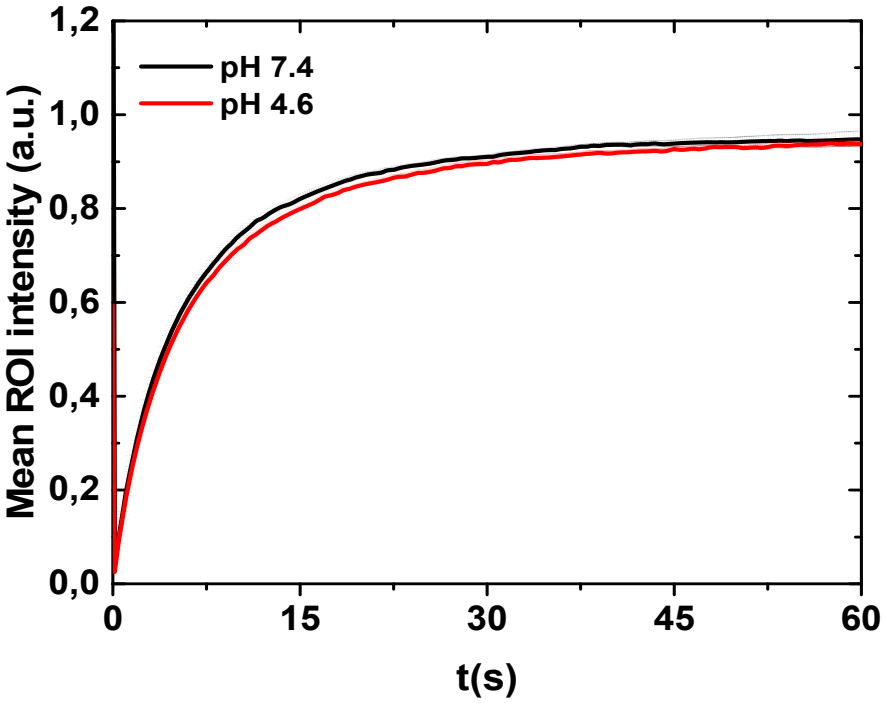

FIGURE S4. Fluorescence recovery after photobleaching on 4% PIP_2-SLBs measured at pH 4.6 and at pH 7.4. The experimental curves were normalized by the fluorescence value before photobleaching. The continuous curves represent the mean fluorescence signal of 12 independent curves from 4 different SLBs.

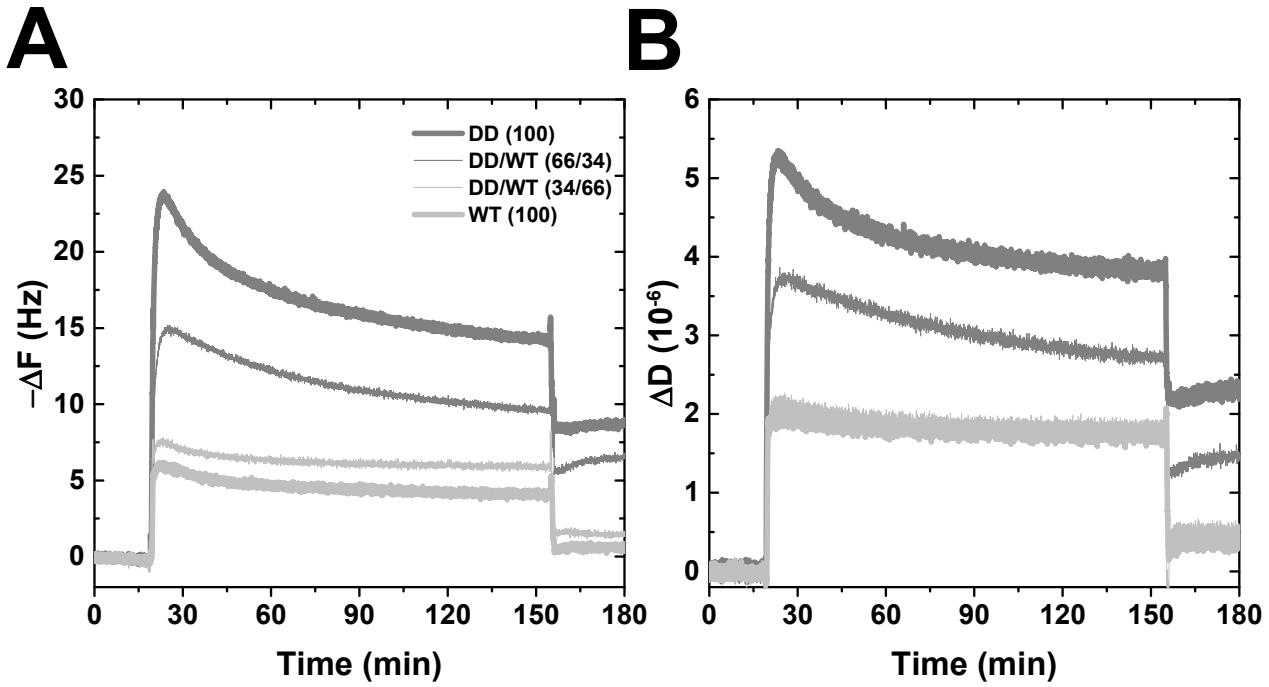

FIGURE S5. Comparison of the adsorption kinetics of WT and DD moesin (at 13.6 µM) on 4% PIP_2-SLBs followed by QCM-D. The quantity of protein bound increases with the % of DD moesin in the protein mixture. (A) Normalized frequency $\Delta f/\nu$ shift acquired at the 3rd overtone of 15 MHz (ν =3). (B) Dissipation shift.

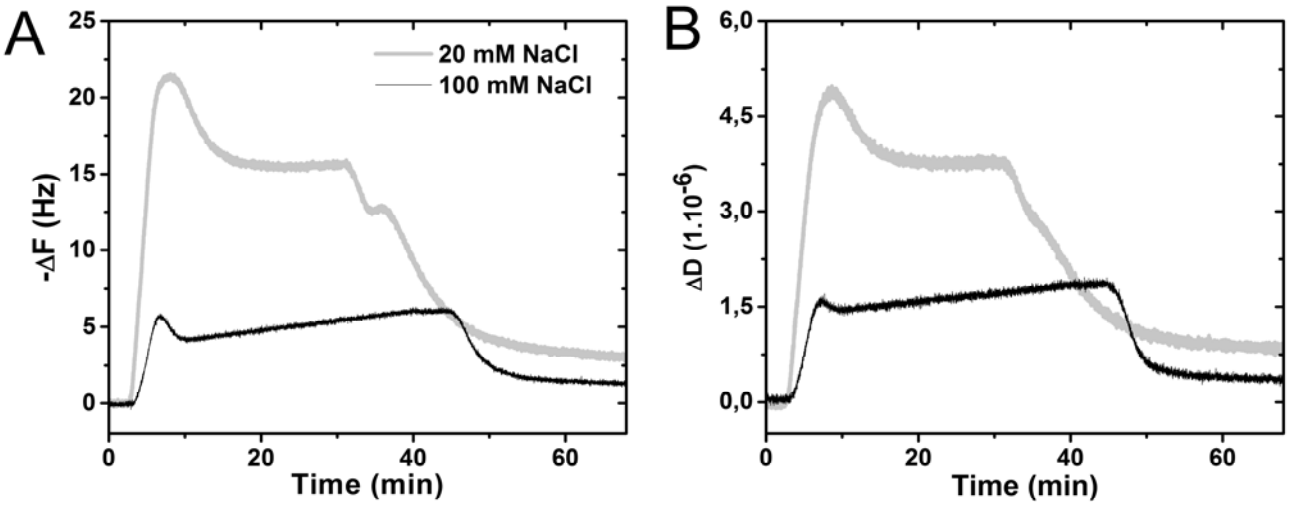

FIGURE S6. Comparison of the adsorption kinetics of DD moesin (at 4 µM) on 4% PIP_2-SLBs followed by QCM-D at two different ionic strength. 20 mM (gray line) versus 100 mM NaCl (black line). Normalized frequency $\Delta f/\nu$ shift acquired at the 3rd overtone of 15 MHz (ν =3) (left) and dissipation shift (right).

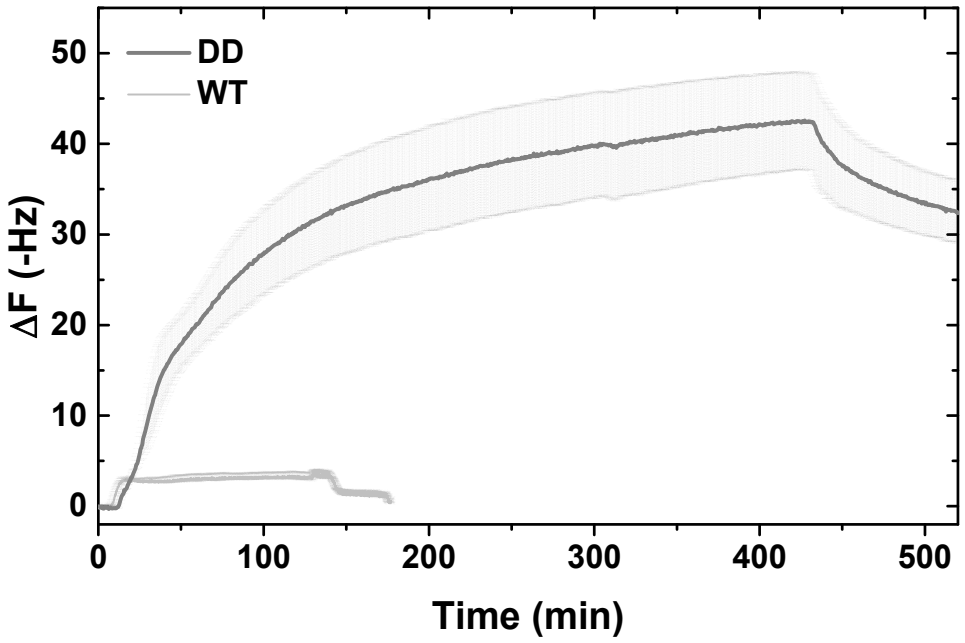

FIGURE S7. Flow-driven adsorption of WT and DD-moesin on 4% PIP_2-SLBs followed by QCM-D. Comparison of the adsorption under flow at 10 µL/min for WT and DD-moesin (at 5 µM). The continuous lines indicate the mean signal and the grey area shows the standard deviations of the measurements. The adsorption of DD moesin is steady and reaches a very high plateau value, while that of WT moesin is very small and fast.